Sustainable Materials and Technologies 45 (2025) e01491

Contents lists available at ScienceDirect

Sustainable Materials and Technologies

journal homepage: www.elsevier.com/locate/susmat

The role of high recycled content and heat treatments on microstructure, mechanical properties, and sustainability for an AlSi10MnMg structural automotive component

Riccardo Arcaleni [a,*], Luca Girelli [b], Lavinia Tonelli [a], Lucia Lattanzi [c], Marialaura Tocci [b], Alessandro Morri [a], Annalisa Pola [b], Lorella Ceschini [a]

[a] University of Bologna, Department of Industrial Engineering, Viale Risorgimento 4, 40136 Bologna, Italy
[b] University of Brescia, Department of Mechanical and Industrial Engineering, Via Branze 38, 25123 Brescia, Italy
[c] Jönköping University, School of Engineering, Department of Materials and Manufacturing, Gjuterigatan 5, 55318 Jönköping, Sweden

ARTICLE INFO

Keywords:
Aluminium
HPDC
Recycling
Tensile
Microstructure
Heat treatment
Environment

ABSTRACT

Secondary aluminum alloys are produced with end-of-life scraps and are gaining importance for environmental sustainability, thanks to their low intrinsic carbon footprint and energy saving compared to the primary ones. They are increasingly used in the automotive sector for large and complex cast components. However, recycled alloys contaminants like Fe promote the formation of brittle intermetallic compounds, which negatively affect tensile strength and ductility. This study compares the mechanical performance and environmental impact of primary and recycled high pressure die casting AlSi10MnMg (EN AB 43500) alloy under as-produced and heat-treated conditions. Samples were extracted from a die-cast automotive component and subjected to annealing and an optimized T6 heat treatment to balance strength and ductility. Microstructural analysis using field emission scanning electron microscopy revealed a similar pores area fraction, as well as shape, size, and distribution of brittle acicular β-Al_5FeSi and polygonal α-$Al_{15}(Fe,Mn)_3Si_2$ Fe-rich phases in the primary and recycled alloys under different heat treatment conditions. This similarity justifies the comparable mechanical behavior of the primary and recycled alloy, characterized by limited ductility in the as-produced condition, often insufficient for safety-critical structural components. Heat treatments significantly improved ductility, increasing it by 40–50 % after annealing and nearly doubling it after T6 due to the fragmentation, spheroidization, and coarsening of the eutectic Si. However, the microstructure change reduces strength by a third after annealing and by 20 % after T6, ultimately influencing the final fracture mechanisms. Moreover, heat treatments increase energy consumption, with annealing and T6 leading to about 25 % and 30 % rises, respectively, making them justified only for elongation enhancement.

1. Introduction

Recent advancements in metal casting technology in the automotive industry have enabled the development of mega-casting or giga-casting [1,2], large-scale components that can integrate multiple smaller components of the body-in-white, underbody structures and chassis into a simple and massive casting. This concept, first implemented in the United States of America [3], streamlines the vehicle assembly process and reduces its overall mass, making it highly suitable for sustainable mobility initiatives. The transition toward mega-castings has driven the development of large automotive components, including electric vehicle (EV) motors, battery housings, knuckle carriers, and shock-towers [4]. These complex thin-walled parts are typically manufactured using high pressure die casting (HPDC) Al-Si-Mg primary alloys due to their high strength-to-weight ratio, excellent corrosion resistance, good wear resistance, superior castability, and cost effectiveness [5]. Primary aluminum, i.e., aluminum extracted from bauxite, has a significant environmental impact, including byproduct disposal, energy consumption, and greenhouse gas (GHG) emissions, mainly associated with the electrolysis stage. In detail, producing 1 ton of primary aluminum ingots requires at least 3.2 tons of dry bauxite and 13–16 MWh of electricity, responsible for about 12 tons $CO_{2\text{-Eq.}}$ [6] and 3.2–3.7 tons of wet red

* Corresponding author.
E-mail address: riccardo.arcaleni2@unibo.it (R. Arcaleni).

https://doi.org/10.1016/j.susmat.2025.e01491
Received 28 February 2025; Received in revised form 13 May 2025; Accepted 11 June 2025
Available online 14 June 2025

mud [7]. On the other hand, the production of secondary aluminum alloys by re-melting aluminum scraps requires about 2.8 MWh emitting only 0.6 tons $CO_{2\text{-Eq.}}$ [8], with a $CO_{2\text{-eq}}$ saving as high as 95 %. Therefore, the European Commission and the automotive original equipment manufacturers (OEMs) are actively promoting the transition to recycled aluminum alloys for structural components.

Nevertheless, there are technological challenges related to remelting: about 20 % of virgin aluminum is added to dilute the recycled material in the new cast products when producing structural car components [9]. About 45 % of material losses occur when aluminum turnings are recycled and most of these losses can be traced to the remelting step due to oxidation and scrap generation. Moreover, two critical aspects of aluminum recycling were identified by Cullen and Allwood [10] that are still relevant: significant dilution with primary aluminum, as above mentioned, and cascade flows of pure aluminum to compensate for the shortfall in scrap supply to obtain the targeted alloy. These points significantly increase the energy required for recycling and cause large value losses because of the downgrading of the material. Important factors for the environmental impact are the additions of alloying elements, such as primary silicon, needed to meet the targeted content in the standard alloy. In fact, Si as an alloying element has an embodied energy of 123–136 MJ/kg and CO_2 footprint of 10–11 $kgCO_{2\text{-eq}}$/kg, with an additional heat of fusion of 1.8 MJ/kg [11].

Moreover, undesired elements such as Fe, Zn, and sometimes Cu increase during secondary processing, especially when high fractions of scrap are recycled. To ensure the production of high-quality components from secondary alloys, well-sorted, cleaned, and pre-consumer scrap is preferably needed as starting material to produce recycled ingots [7]. Despite a limited Fe content (up to 0.55 % for the well-known AlSi10Mg [12]) being necessary in HPDC to prevent the die soldering phenomenon during the casting process [13], it is crucial that the Fe content does not exceed 0.25 % in structural automotive components requiring high ductility and yield strength, such as shock-towers [14].

Fe is considered harmful for ductility and, also, fatigue strength due to its ability to form complex and brittle intermetallic compounds, such as the acicular β-Al_5FeSi phase [15]. As the Fe content increases, the equivalent diameter of Fe-rich phases also grows [16], and due to their platelet-like morphology, these compounds act as sites for stress concentration and facilitate crack propagation. The results are premature failure of castings and reduced energy absorption during a crash, with Fe content being therefore a key factor in limiting the use of secondary aluminum alloys for structural components [8]. The addition of neutralizing elements, typically Mn and Cr, can mitigate the needle-like phase by promoting the formation of compact α-$Al_x(Fe,Mn,Cr)_ySi_z$ phases with script-, polygonal- or star- like morphologies [14,17], depending on the concentration of Mn and Cr. The literature suggests that a Mn content of at least half that of the Fe concentration (Mn/Fe ratio > 0.5) is required to tolerate high Fe (> 0.4 wt%) alloys [14]. Bösch et al. [13] recommended maintaining a Mn/Fe ratio of at least 1 to promote the formation of fine-sized α-$Al_{15}(Fe, Mn)_3Si_2$ phases, with size and morphology comparable to modified eutectic silicon, which does not alter the fracture mechanisms. In contrast, excessively low or high Mn/Fe ratio leads to the formation of, respectively, β-phases and large primary Fe-based particles, known as sludge [17]. These phases fracture under load, resulting in de-cohesion and void formation within the matrix.

The Gobrecht [18] and Jorstad [19] Sludge or Segregation Factor (SF) models predict sludge formation based on the following empirical eq. SF = (1 * wt% Fe) + (2 * wt% Mn) + (3 * wt% Cr). To prevent sludge formation in the holding furnace at about 650 °C, an SF below 1.8 is strongly recommended [13,17]. This challenge has driven the development of specially designed alloys that maintain a favorable SF, thereby minimizing or avoiding the formation of β-Fe needle and sludge phases, as seen in the well-studied AlSi10MnMg alloy [20,21]. This alloy was originally developed as a primary alloy, in accordance with EN AC 43500 [12], for die casting processes. However, its variants from scrap recycling are currently also being investigated [22].

This interest arises from the fact that cooling rate significantly influences the type and size of intermetallic particles, potentially reducing their dimensions or altering their morphology, which makes the use of secondary alloys increasingly feasible. Cinckilic et al. [21] noted that high cooling rates, such as those in HPDC, combined with an Mn/Fe ratio of 1.6 to 3.0, can drastically reduce the formation of β-phases, resulting in the development of Fe-rich phases (polyhedral intermetallic compounds as primary α_I and secondary α_{II} phases) and eutectic Fe-rich phases (plate-shaped, net-like, and fishbone-shaped) [23].

However, the inability to efficiently eliminate contaminants in recycled alloy necessitates the use of customized heat treatments to enhance the mechanical properties, especially the ductility. Annealing, for instance, reduces hardness by softening the aluminum matrix and relieving residual stresses induced by the casting process [24]. On the other hand, it is not suitable for inducing precipitation hardening. The well-known heat treatment that improves tensile strength and elongation in Al-Si-Mg sand and permanent mold castings is the T6 one consisting of solution, quenching, and artificial aging. Adjustments to the heat treatment parameters are however often necessary when applying the T6 treatment to HPDC components, as the latter involves process-induced porosity. According to Hu et al. [25], voids enlarge during solution heat treatment, leading to blistering phenomena and compromising structural integrity [26]. For this reason, short and low temperature (< 500 °C) solution treatments are typically performed on HPDC parts. Hence, in general, optimizing T6 parameters is critical to ensure good material properties and prevent blistering [27].

Based on the presented literature, there is a need to optimize the heat treatment on recycled aluminum alloys for HPDC components. The heat treatment response depends on the composition and microstructure, which can vary locally due to the cooling rate of the process, also considering possible different thickness.

The aim of this study is to determine the most suitable heat treatment conditions for both primary and high-recycled content HPDC AlSi10MnMg alloy, by comparing their tensile properties and failure mechanisms. Microstructural and mechanical characterizations were performed on samples extracted from two shock-towers produced by HPDC using, respectively, primary and high-recycled (at least 70 %) content AlSi10MnMg alloy. By using commercially available alloys and real components, this study demonstrates practical applicability to mass production, with heat treatment parameters adaptable to existing production plants. A detailed microstructural analysis, with particular focus on the eutectic and Fe-intermetallic phases, was conducted on both as-produced and heat-treated samples to explore the correlation with the resulting mechanical behavior and fracture mechanisms. In addition, the environmental impact related to the used alloy (primary or high-recycled) and the different processing routes (as produced and heat treated) on the shock-tower life were evaluated. Through this comprehensive analysis, the impact of material choice and heat treatment on the end-of-life potential will be evaluated, including simulations of the component's use and transportation phases.

2. Materials and methods

2.1. Materials and heat treatments

The experimental activity of this work was carried out on samples extracted from two automotive components produced by HPDC using, respectively, primary (P) and high-recycled content (HR) AlSi10MnMg (according to EN AC 43500 specification) alloy. In particular, P alloy was produced from primary ingots with the addition of up to 40 % of internal returned alloys, originating from runners, overflows, and rejected die castings, in accordance with the specifications reported in foundry datasheets [28,29], which typically limit their use to a maximum of 40–50 %. The HR alloy, instead, qualifies as a recycled material because it was obtained from scrap sourced from post-

consumer components, remelted into secondary ingots, and reintroduced into the production cycle, thus completing a closed-loop of use and recovery, with the same maximum content of internal returned [29].

The cast components analyzed were two shock-towers produced for a premium car. These structural components are being increasingly manufactured by HPDC rather than low pressure die casting or gravity casting for reduced thickness, which results in lower material consumption and lightweighting.

After the casting process, the components were cooled in water at room temperature to facilitate the trimming of runners and overflows. The components were stored at room temperature, without any heat treatment, for at least 1 month before testing in order to facilitate the possible natural aging phenomenon. This condition is referred to as-produced (AP) in the current study.

Table 1 reports the chemical composition of the two alloys evaluated by a Glow Discharge Optical Emission Spectroscope (GD-OES) (GDA 650, Spectruma Analytik GmbH, Hof in Bayern, Germany) according to ISO 14707:2015 [30] on an area of approximately 20 mm^2. Chemical composition of P and HR AlSi10MnMg alloy (also designated as EN AC 43500) complied with the EN 1706:2020 standard. The HR alloy presents a slightly higher Fe content compared to the primary alloy, an inevitable consequence of using recycled material, which positively contributes to mitigate the die soldering phenomenon. Both alloys were modified with Sr (avg. 0.012 % for P alloy; avg. 0.010 % for HR alloy) to enhance the spheroidization of the eutectic Si, and grain refined with Ti-B as confirmed by the presence of Ti in Table 1.

For both P and HR alloy, the Zn was slightly higher in comparison with the range requested by the standard. In order to evaluate the chemical composition of the alloy also considering a greater volume than in GD-OES analysis, an overall mass of at least 0.1 kg was taken from different areas of each casting, melted, solidified and analyzed with an arc/spark optical emission spectrometer. The results confirmed those obtained previously except for the Zn which is significantly lower in this case and complies with the standard limits (avg. 0.002 % for P alloy; avg. 0.013 % for HR alloy). This discrepancy may be attributed to differences in the investigated area or instrument calibration for Zn detection.

Samples for microstructural analyses and mechanical testing were extracted from both castings from areas with a thickness of approximately 3 mm to ensure similar cooling conditions. Some samples were analyzed in the as-produced condition, while others underwent annealing and T6 heat treatments.

The annealing (AN) consisted of soaking the alloy at 380 °C for 200 min (with the cold specimen placed into the preheated furnace), followed by cooling to room temperature in calm air. These parameters were selected based on a similar study found in the literature [24] in which samples were heat-treated at temperatures between 350 °C and 450 °C for 180 min.

The T6 parameters were identified as the optimal time-temperature combination from a range of tested conditions, achieving a balance between improved mechanical properties, minimal distortions, and avoiding excessively long durations or high aging temperatures. In detail, to reduce the risk of casting distortions that could make the components unusable, caused by prolonged exposure to high temperatures (around 500 °C) for extended durations (over 60 min) and excessively rapid quenching, the T6 heat treatment was applied to samples with approximate dimensions of 20 mm × 20 mm, according to the following procedure:

a. Solution of 45 min including:
   a. 1st step: 460 °C for 30 min inserting the sample (at room temperature) in a preheated furnace;
   b. 2nd step: 470 °C, 480 °C, or 490 °C for 10 min with a heating of 5 min from the 1st step.
   c. Quenching in forced air
   d. Aging at 190 °C, at 210 °C, or at 230 °C for 60 min or 90 min.
   e. Cooling after aging in calm air.

A sketch of the solution and quenching treatments is reported in Fig. 1.

The relatively low solution treatment temperature, compared to other Al-Si-Mg HPDC alloys [31], avoids the risk of blistering [27]. The air quenching was chosen, despite the possible lower effectiveness, to avoid the risk of distortions induced by high residual stresses on thin-walled castings in the case of water quenching.

The hardness was measured according to Brinell method using a LTF Galileo Ergotest Comp25 apparatus with a WC ball (diameter of 2.5 mm). In detail, a load of 613 N (62.5 kgf) was applied for 5 s and maintained for 15 s. On each sample, 4 indentations were performed, and both average values and standard deviation were calculated.

The density of the sample was measured by the hydrostatic method, using a laboratory weighting scale (Radwag, AS 220.R2 Plus, Radom, Poland), with a specific sample holder, measuring the mass in both air and deionized water. A density of 1.0 g/cm^3 was assumed for the deionized water. To evaluate the effect of the T6 parameter on the alloys, the density was measured twice on the same sample, once under as-produced condition and again after the T6 treatment. It should be considered that results can be affected by the possible presence of air bubbles between the specimen and the sample holder that cannot be detected by the operator.

2.2. Microstructural characterization, and thermodynamic simulations

A comprehensive microstructural characterization was carried out by optical microscopy (OM) (Zeiss, AXIO, Oberkochen, Germany) and Field Emission Gun Scanning Electron Microscopy (FEG-SEM) (Tescan, MIRA3, Brno, Czech Republic) equipped with Energy-Dispersive X-ray Spectroscopy (EDS) (Bruker, Billerica, MA, USA). Samples were prepared using standard metallographic procedures, including surface polishing up to 1 μm and chemical etching with Keller's reagent (1 vol% HF, 1.5 vol% HCl, 2.5 vol% HNO_3 and 95 vol% H_2O) for 10 s. The analysis focused on comparing the microstructure of P and HR alloy in both as-produced and heat-treated conditions. A quantitative analysis was performed on the core regions of the samples, away from the surface or skin layer, to evaluate secondary dendrite arm spacing (SDAS), eutectic silicon, intermetallic compounds and defects. For each alloy and condition, the SDAS value was calculated by averaging data from at least 6 images taken from the core regions of the samples, with the field of

Table 1
Chemical composition measured by GD-OES directly on samples taken from the casting. The standard deviation is reported in round brackets.

AlSi10MnMg	Si	Fe	Mn	Mg	Zn	Ti	Cu	Cr	Other		Al
Alloy									Each	Total	
P	9.672 (0.382)	0.127 (0.01)	0.579 (0.024)	0.320 (0.018)	0.071 (0.004)	0.052 (0.003)	0.001 (0.001)	0.000 (0.000)	<0.013 (0.003)	0.088 (0.029)	Bal.
HR	10.187 (0.071)	0.153 (0.005)	0.604 (0.02)	0.367 (0.020)	0.083 (0.007)	0.059 (0.001)	0.027 (0.001)	0.005 (0.000)	<0.015 (0.004)	0.071 (0.015)	Bal.
EN AC 43500 [12]	9.0–11.5	< 0.25	0.4–0.8	0.1–0.6	< 0.07	< 0.20	< 0.05	< 0.05	<0.050	<0.15	Bal.

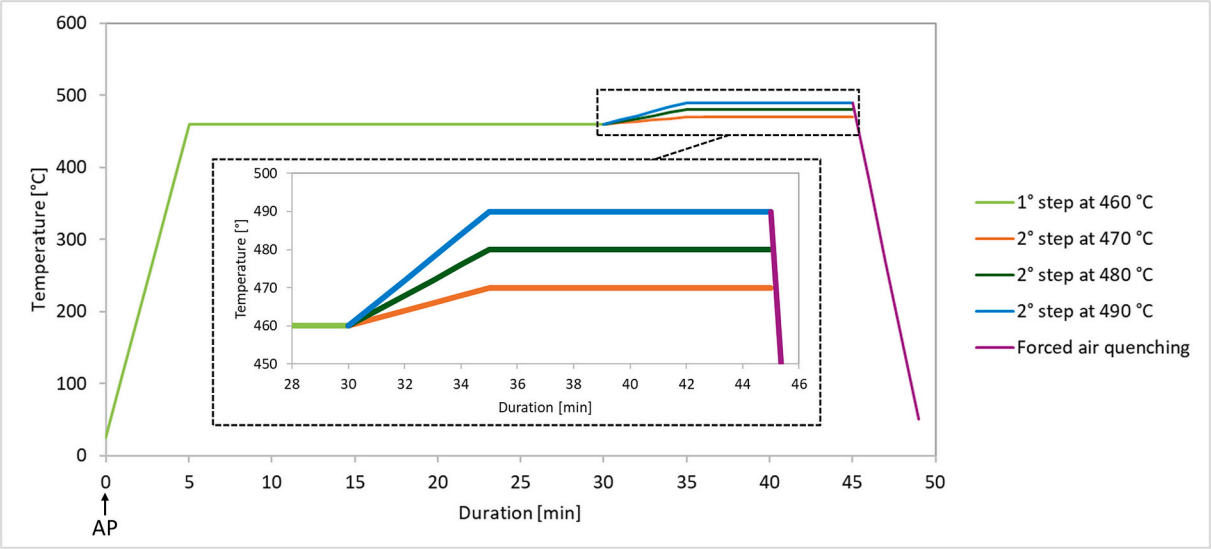

Fig. 1. Sketch of solution and quenching treatments for the T6 optimization.

view of 350 × 200 μm, with a minimum of 10 SDAS measurements per image. The total area investigated for defect analysis was about 200 mm^2 per sample. The analysis of the eutectic Si particles size, morphology and distribution was carried out on 10 SEM images with the field of view of 10.4 × 10.4 μm for the as-produced condition and 5 images with the field of view of 20.8 × 20.8 μm for the annealed and T6 conditions, for both P and HR alloy (total investigated area ≈ 1080 μm^2). The Feret diameter, defined as the longest distance between any 2 points along the object boundary [32], was used as representative of the size of eutectic silicon particles. For morphology characterization, the Aspect Ratio (AR) (Eq. 1) was employed, which is defined as the aspect ratio of the particles fitted ellipse or the inverse of the Roundness (Eq. 2), and the spacing (Eq. 3) for the mean distance between particles, i.e. the distribution.

$$AR = \frac{Major\_Axis}{Minor\_Axis} \tag{1}$$

$$Roundness = \frac{4A}{\pi Major\_Axis^2} \tag{2}$$

$$Spacing = \sqrt{\frac{A}{N}} \tag{3}$$

In eq.3, A is the total investigated area and N the particles number. The samples under as-produced, annealed and optimized T6 conditions were subjected to the hardness characterization according to the previously reported methodology used for the T6 optimization.

Moreover, thermodynamic simulations were conducted using Thermo-Calc, version 2024b [33], with the TCAL8: Al-Alloys v.8.2 database to thoroughly investigate the nature and quantity of the main phases present in the microstructure. Scheil and equilibrium graphs were built for both P and HR alloys through the average value of the main constituent elements taken from Table 1.

2.3. Tensile tests and fractography

Tensile testing was performed using an Instron 3369 machine with a 50 kN load cell and Bluehill software for control purposes. The castings were divided into smaller sections and subjected to annealing and optimized T6, while maintaining the as-produced condition as a reference for comparison. The specimens featured the following dimensions: 107 mm total length (L_f), 25 mm gauge length (L_0), and 12.00 mm fillet radius (r) connecting the gauge section with the ends, in agreement with UNI EN ISO 6892-1:2016 standard [33]. The gauge section thickness (a_0) measured 2 mm. Tests were conducted at room temperature, allowing for contact mechanical extensometer use, under displacement control with a 1 mm/min constant strain rate. The stress-strain curves accounted for the pre-load from the upper and lower grip clamping. For excessive elongation beyond extensometer capability, analysis relied on crosshead displacement data. A minimum of two samples were evaluated for each condition.

A comprehensive fractographic analysis was conducted to evaluate how heat treatment parameters and recycling affected the fracture mechanisms in HPDC AlSi10MnMg alloy. This investigation employed SEM-EDS techniques to analyze both fracture surfaces and cross-sectional samples with embedded fracture surfaces, enabling identification of the primary failure mechanisms. This methodology provided thorough insights into the microstructural features responsible for fracture behavior across various heat treatment routes and alloy compositions.

2.4. Environmental impact assessment

The Eco Audit tool in the Granta Software (2023 R1, version 23.1.1) was used to assess the environmental impact of the material and the processing steps on the overall product life of a shock tower. The data used are detailed in Appendix A. The embodied energy and CO_2 footprint of the HR alloy were retrieved from the Silval alloy Environmental Product Declaration (EPD) by Raffmetal S.p.A. [11], and the energy consumption related to the heat treatment were measured through an Electric Energy Current Meter coupled to a muffle furnace (Nabertherm Gmbh, Nabertherm Lt 9/14, Lilienthal, Germany). All the other data were retrieved from the Granta Selector database included in the software.

3. Results and discussion

3.1. T6 heat treatment optimization

The hardness of the samples measured after all the T6 tested conditions are reported in Fig. 2 in comparison with the data of the as-produced specimen. No substantial differences were observed between P and HR under any of the tested conditions. As expected, samples subjected to the highest temperature solution heat treatment exhibited slightly higher hardness values. Moreover, the slightly higher hardness of HR compared to P may be attributed to its slightly higher Fe content

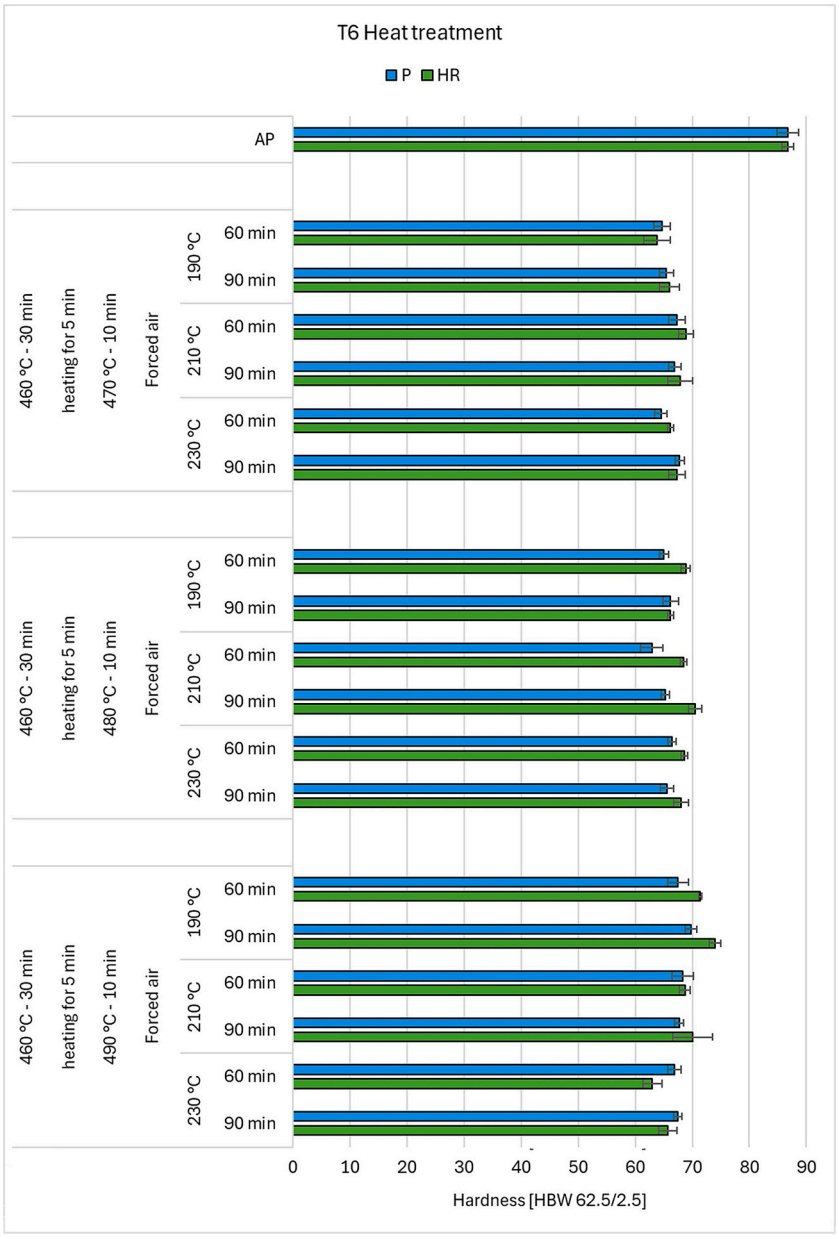

Fig. 2. Effect of T6 heat treatment parameters on the hardness of P and HR alloy, compared with the AP one.

(Table 1). Notably, no blistering phenomena were detected under these T6 conditions.

The density of the samples measured after all the T6 tested conditions are reported in Table 2 in comparison with the data of the as-produced specimen. For both the P and HR alloy, the values for the AP condition were calculated as the average value of the measurements performed on 18 samples for each alloy before the heat treatment.

The samples subjected to the T6 with the 2nd step of solution at 490 °C showed the greatest decrease in density, likely due to the enlargement of the gas porosity, a common feature in HPDC. Elevated temperatures and extended exposure times, in fact, cause an increase in gas pressure within the pores, accompanied by a reduction in alloy strength, which in turn leads to larger pore sizes, as reported by Di Egidio et al. [34]. In contrast, the samples treated with the 2nd step of solution at 470 °C exhibited minimal variation in density.

Based on the analyses of both hardness (Fig. 2) and density (Table 2) results, the T6 treatment consisting in a 1st solution step at 460 °C for 30 min, followed by a 2nd solution step at 470 °C for 10 min (with 5 min heating period), quenching in forced air and aging at 210 °C for 60 min was identified as the optimal balance between hardness and density for both the P and HR alloy. Furthermore, considering the temperature difference between the 1st and the 2nd step of only 10 °C, and with the goal of simplifying the treatment for industrial application, the optimized T6 heat treatment can therefore be implemented as follows:

a. solution (only 1 step) at 470 °C for 45 min (inserting cold samples in preheated furnace);
b. quenching in forced air;
c. aging at 210 °C for 60 min (inserting cold samples in preheated furnace).

3.2. *Microstructural characterization*

The AlSi10MnMg alloy microstructure is mainly composed of α-Al matrix surrounded by the eutectic Al-Si mixture for both primary and recycled alloy (Fig. 3). Both P and HR alloys were found to contain

Table 2
Effect of T6 heat treatment parameters on the density of P and HR alloy, compared with the AP one.

Solution			460 °C - 30 min heating of 5 min 470 °C - 10 min	460 °C - 30 min heating of 5 min 480 °C - 10 min	460 °C - 30 min heating of 5 min 490 °C - 10 min
Quenching			Forced air	Forced air	Forced air
Aging			n. 6 aging conditions	n. 6 aging conditions	n. 6 aging conditions
P	AP	g/cm^3	2.675	2.684	2.682
	T6	g/cm^3	2.675	2.665	2.656
	var.	%	0.00 %	−0.71 %	−0.97 %
HR	AP	g/cm^3	2.665	2.669	2.669
	T6	g/cm^3	2.666	2.663	2.660
	var.	%	+0.04 %	−0.22 %	−0.34 %

intermetallic phases, predominantly enriched with Fe and Mn along with Mg_2Si compounds, the latter observed exclusively in the as-produced condition. The α-Al phase is present in the form of fine dendrites or small rosettes and, occasionally, in the form of randomly distributed large particles, which in the literature are referred to as Externally Solidified Crystals (ESC) [35]. No significant changes in shape or size of the α-Al phase are noticeable between the P and HR alloy neither after the annealing nor after the T6 heat treatments.

Fig. 4.a illustrates that the mean SDAS values in the AP condition were approximately 5 μm for both P and HR, which is characteristic of thin-walled castings produced by HPDC technology, where SDAS typically ranges from 5 to 10 μm [35]. After AN and T6 heat treatments, the SDAS values remain around 5–6 μm, with variations that fall within the measurement deviation, making them comparable to the AP condition.

In terms of defects, the results showed a similar value for both P and HR in the as-produced condition (AP), with a pores area fraction of less than 0.1 % detected across a total examined area of 200 mm^2 per sample (Fig. 4.b). Heat treatments (AN and T6) caused a slight increase in pores area fraction, reaching a maximum of approximately 0.3 %, especially in HR alloy. The higher defect density in HR compared to P alloy is consistent with findings in the literature [16]. One of the reasons may be that the liquid Al melt containing a higher fraction of returned alloys or recycled materials tends to have a higher oxide content, which can promote porosity formation, as oxides may act as nucleation sites for pores during the solidification of Al castings according to Campbell [36]. The investigated gas and shrinkage pores have a maximum size of roughly 300 μm in both P and HR alloys.

The high-magnification SEM-FEG images (Fig. 5) provide a clear view of the microstructure of the eutectic region. For both P and HR as-produced conditions, the eutectic silicon particles were effectively modified by the presence of Sr, leading to a fine fibrous morphology. This helps reducing the stress concentration at the sharp corners of the silicon lamellae, enhancing the alloy overall mechanical properties, especially the elongation, as reported by Ganesh et al. [37].

Qualitatively, it is evident that the eutectic Si particles undergo morphological changes after heat treatment. This variation was

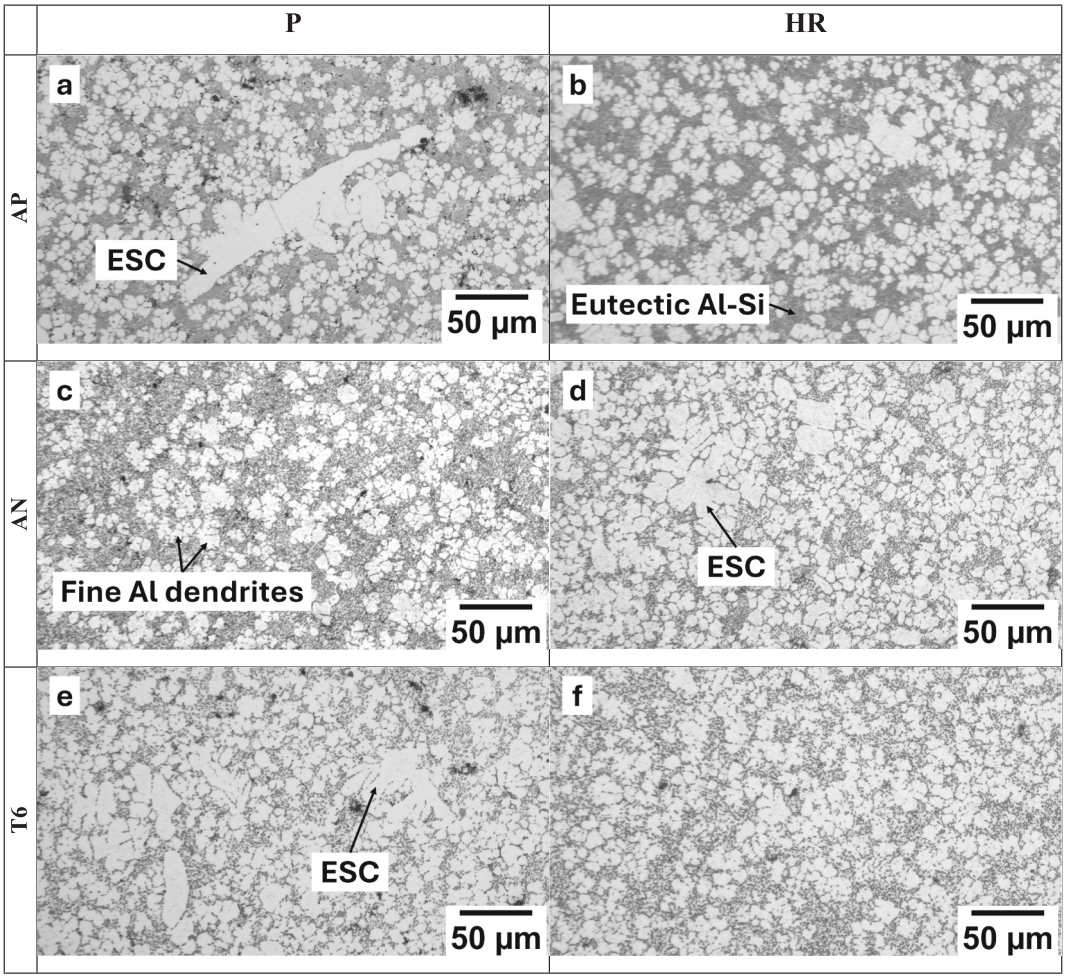

Fig. 3. Optical micrographs of the HPDC P (a, c, e) and HR (b, d, f) AlSi10MnMg alloy microstructure in different conditions: (a, b) AP; (c, d) AN; (e, f) T6.

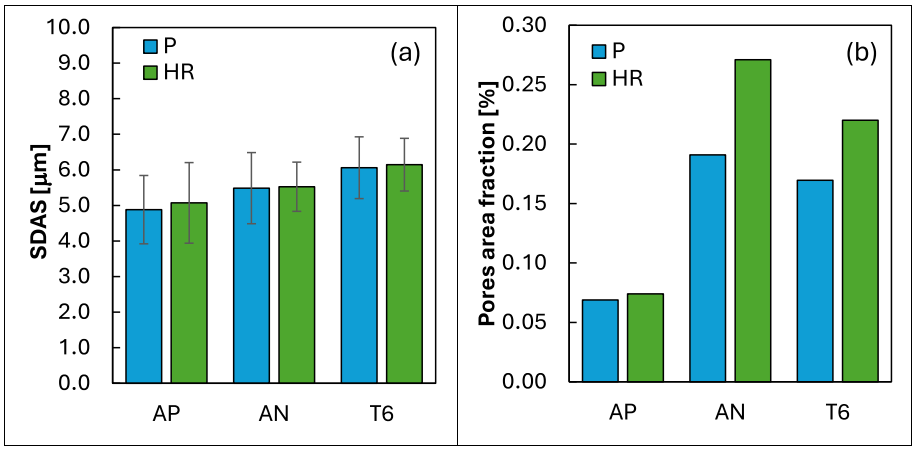

Fig. 4. Result of the quantitative analysis on a) SDAS and b) Pores area fraction measured on metallographic section of primary (P) and high recycled (HR) AlSi10MnMg, in the as produced (AP) and heat treated (AN and T6) conditions.

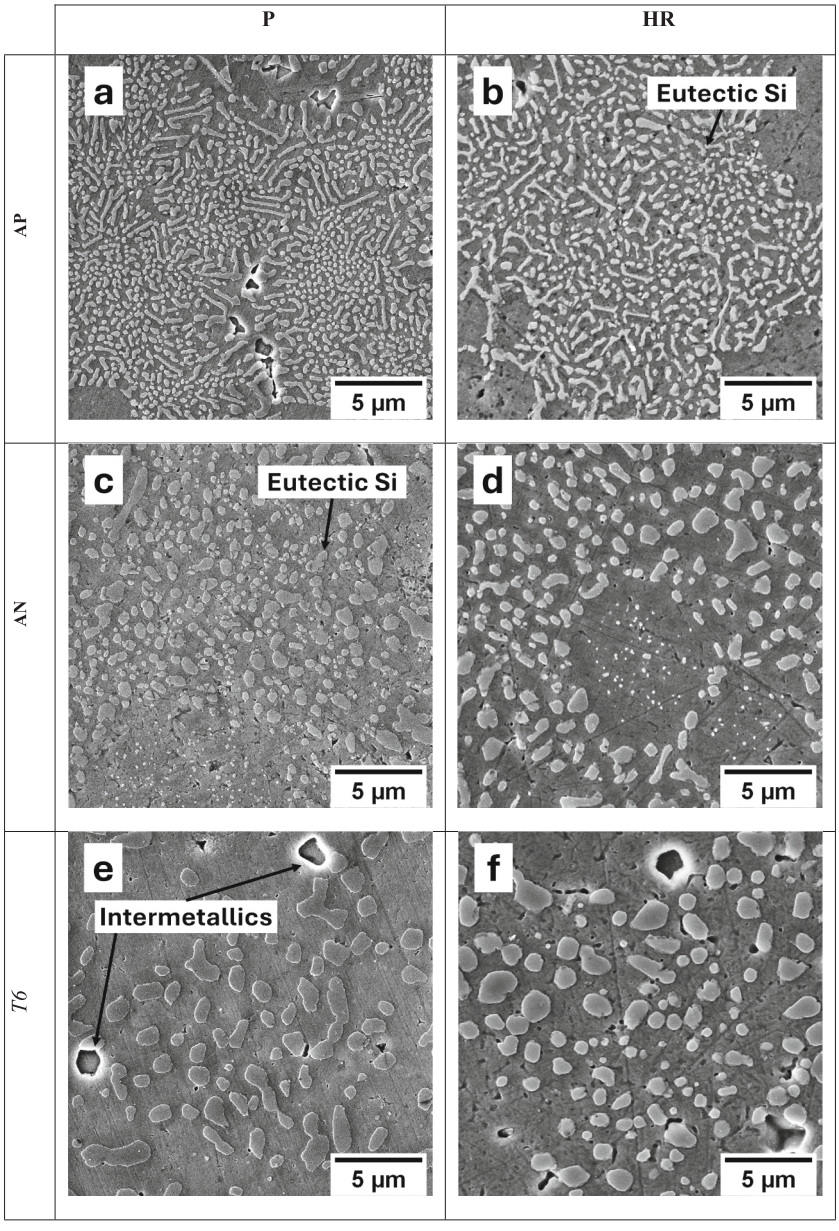

Fig. 5. SEM micrographs of the HPDC P (a, c, e) and HR (b, d, f) AlSi10MnMg alloy microstructure in different conditions: (a, b) AP; (c, d) AN; (e, f) T6.

subsequently measured through a quantitative analysis conducted over an area of about 1 mm^2, confirming an increase in the mean Feret diameter and, thus, in the average Si particle size (Fig. .b).

In particular, there is no distinguished variation of size and morphology of Si particles between the primary (P) and high recycled content (HR) alloy in the AP condition (Fig. 6.b,c,d). It has been noticed that the Feret of eutectic Si particles becomes 40–80 % larger after annealing and nearly doubles following the T6 heat treatment (Fig. 6.b) for both P and HR alloys. Despite the increase in individual eutectic Si particles' size, their area fraction in the eutectic region decreases from approximately 25–30 % in the AP to about 15–20 % after T6 for both P and HR AlSi10MnMg alloy (Fig. 6.a). The reason is that solution treatment of AlSiMg casting alloys dissolves Mg_2Si and Si particles into the Al matrix, forming supersaturation and subsequent nanosized precipitates, thus leading to a reduction in the area fraction of Si particles in the T6 condition compared to the AP.

The heat treatments (AN and T6) resulted also in eutectic Si spheroidization and in an increase of the interparticle spacing (Fig. .c-d). The as-produced alloy features denser Si particles distribution, with some particles displaying greater Feret (Fig. 6.b), indicated by a higher aspect ratio. However, the T6 heat treated HR alloy consistently exhibits slightly lower values, whereas in the AN condition, they are always slightly higher.

In summary, following annealing and T6 heat treatments, the eutectic Si transforms into a coarser and more spherical shape, as illustrated in (Fig. 6). According to Lin et al. [38], this occurs as smaller Si particles dissolve under heat treatment, with their atoms diffusing and adhering to larger particles [39], which, when in proximity, merge to minimize interfacial energy. An enhanced ductility should be achieved after this microstructural modification in accordance with Lee et al. [40].

3.3. Intermetallic compounds

The solidification process and the related variation of liquid compositions regulate the development of intermetallic phases and microstructural features. The Scheil model, which assumes negligible diffusion in solid phases and infinitely fast diffusion in the liquid, can be used to predict the solidification process in HPDC [23]. Fig. 7 presents a Scheil simulation for the P and HR alloy considering the formation of phases from the following elements: Al, Si, Fe, Mn, and Mg. Given the high cooling rate typical of HPDC, solidification occurs under non-equilibrium conditions, making the assumptions of the Scheil model - such as homogeneous liquid composition - more appropriate for simulating real solidification processes compared to equilibrium calculations. The predicted solidification sequence showed that the α-Al phase starts to solidify from the liquid in the P alloy around 595 °C, while the HR alloy presents α-$Al_{15}(Fe,Mn)_3Si_2$ as the first phase to nucleate slightly above 590 °C. However, the amount of solid α-$Al_{15}(Fe,Mn)_3Si_2$ phase that nucleates before aluminum dendrites start nucleating in HR is infinitesimal. Apart from that, the two solidification curves display a similar behavior, promoting then the solidification of the eutectic Si phase and the intermetallic phases, including α-$Al_{15}(Fe,Mn)_3Si_2$, β-Al_5FeSi, Mg_2Si and π-$Al_8FeMgSi_6Al$. The latter is detected by Scheil curves, even if it is not present at room temperature according to the Thermo-Calc equilibrium calculation.

What is observed instead through experimental data, and aligns with the prediction of the Scheil curve, is the formation of the Mg_2Si phase. This phase was observed exclusively in the as-produced condition (Fig. 8.a), while it was absent in both the annealed and T6-treated samples. During annealing, Mg_2Si likely undergoes dissolution, with Mg and Si atoms dispersing into the Al matrix without re-precipitating due to the lack of a subsequent aging step. In contrast, after T6 treatment, the Mg_2Si phase dissolves and re-precipitates as nanosized

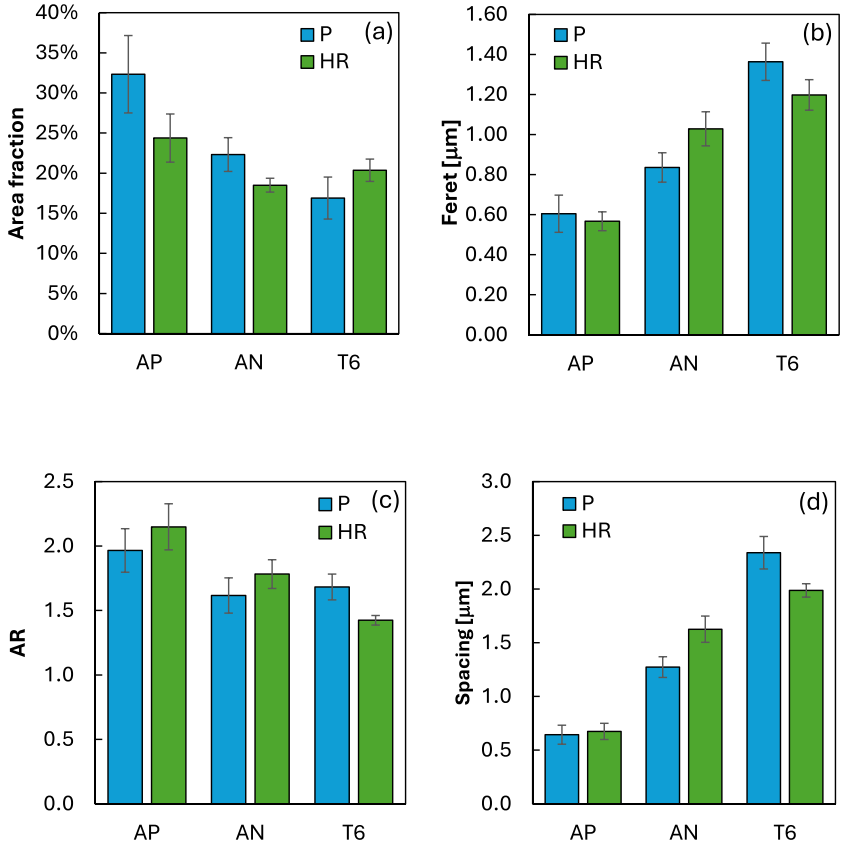

Fig. 6. Results of the eutectic silicon particles characterization on primary and recycled AlSi10MnMg in terms of: a) Area fraction; b) Feret; c) AR; d) Spacing.

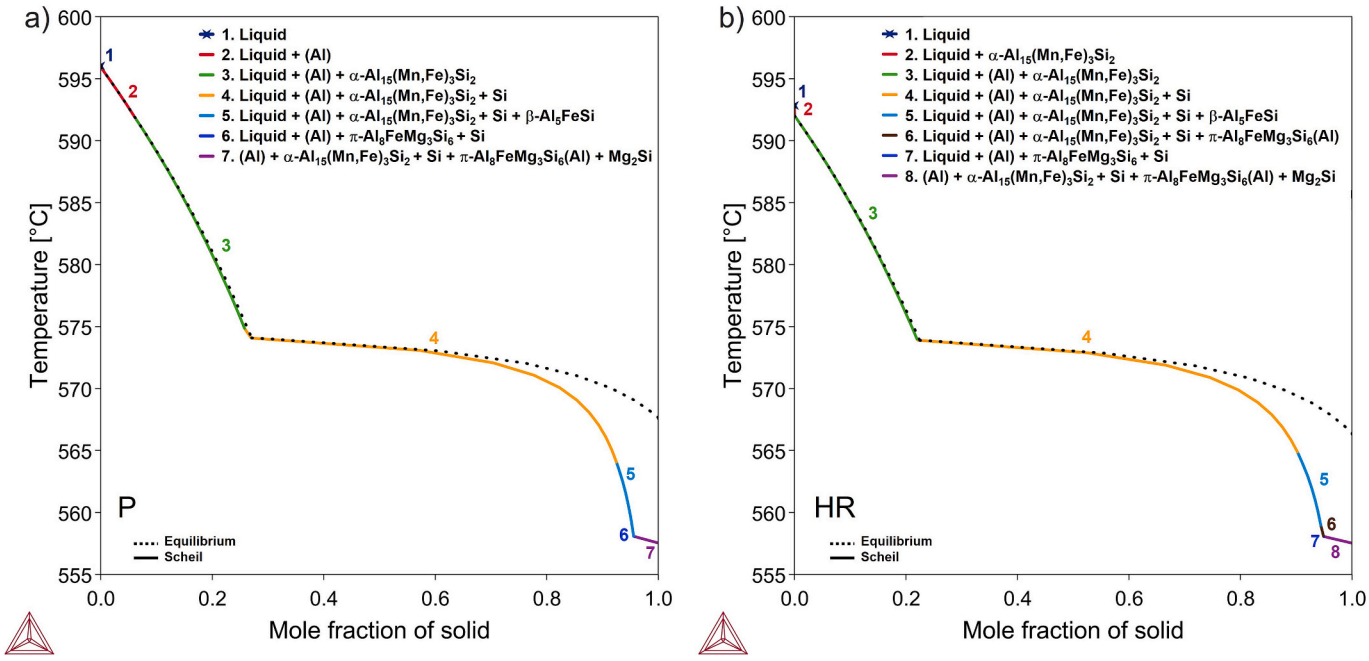

Fig. 7. Equilibrium and Scheil curves for both the P (a) and HR (b) AlSi10MnMg alloy.

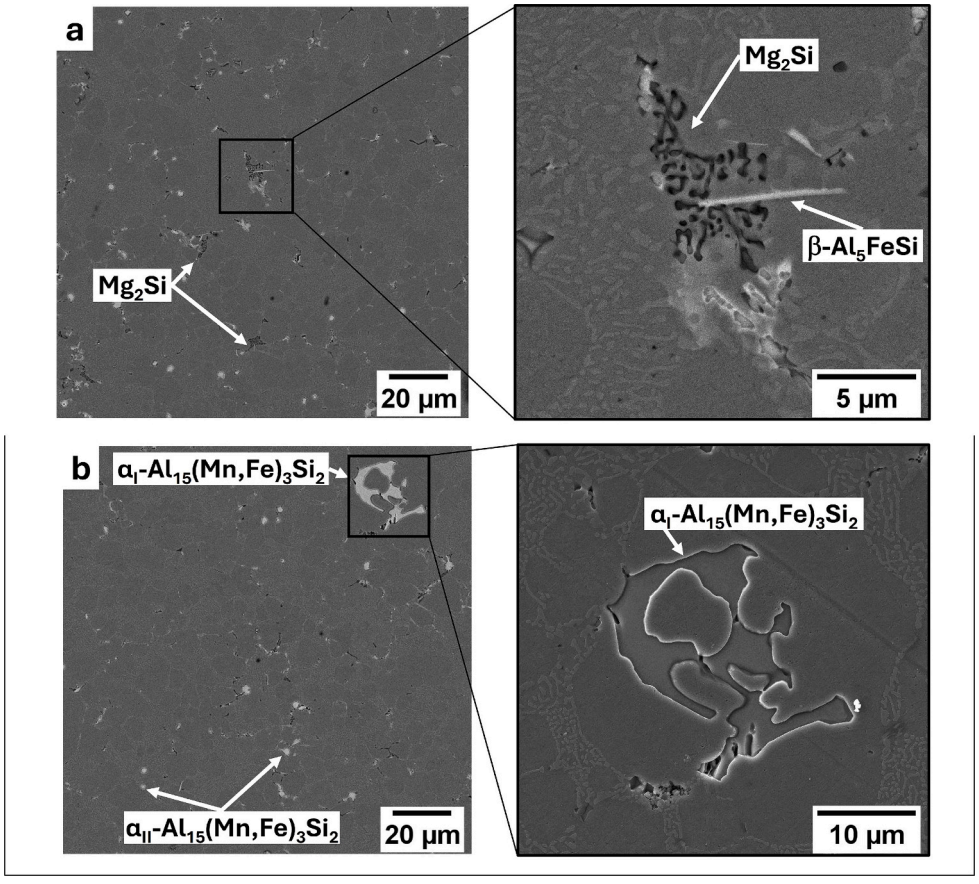

Fig. 8. Different types of intermetallic visible at low and high magnification using SEM- FEG in the AP AlSi10MnMg HR alloy: a) Mg_2Si and β-Al_5FeSi phases; b) $\alpha_{I,II}$-$Al_{15}(Fe,Mn)_3Si_2$.

particles, which are undetectable by OM and SEM-FEG, but align with findings in the literature [22,41], and are supported by the measured mechanical properties.

The thermodynamic simulations findings align with the work conducted by Sanchez et al. [20] on the AlSi10MnMg(Fe) alloy (having 9.5 wt% Si, 0.5 wt% Mn, 0.1 wt% Mg and balanced Al) who show that, after

equilibrium solidification, the microstructure should contain different intermetallic phases depending on the Fe content. In the present paper, the P and HR alloy exhibited a Mn/Fe ratio and Sludge factor (Table 3), calculated based on the average Mn, Fe, and Cr content reported in Table 1, within a range where a predominant presence of the α-$Al_{15}(Fe,Mn)_3Si_2$ phase is expected.

This phase appears in two distinct forms in the microstructure, as α_I-$Al_{15}(Fe,Mn)_3Si_2$ and α_{II}-$Al_{15}(Fe,Mn)_3Si_2$, respectively (Fig. 8.b) for both P and HR. These forms differ based on whether they nucleate before or after the eutectic silicon phase begins to solidify. Specifically, the α_I-$Al_{15}(Fe,Mn)_3Si_2$ phase likely nucleates at higher temperatures within the shot sleeve or during the transfer from the cold chamber to the shot sleeve, as reported in [35]. This phase exhibits a complex polygonal morphology, as it continues to grow during solidification, resulting in large particles approximately 20–50 μm in size, consistent with observations by Bongiovanni et al. [42]. Wang et al. [43] explain the evolution mechanisms of primary α-Fe intermetallic compounds in AlSiMgMn alloys where their shape initially grows as a polyhedron with ⟨100⟩ orientation, progressing to dodecahedron with {110} faces, then to a hexahedron with {100} faces. Further growth results in dendritic arms along ⟨111⟩, forming octagonal dendrite shape. The intermetallic in Fig. 8.b exhibits a hollow structure in space, which could indicate an intermediate stage of its growth. If these particles form before the molten metal is injected into the die, the flow may deform their structure, leading to irregularly shaped particles (Fig. 8.b), moving from the surface to the center of the casting [35]. Therefore, the nucleation zone of those particles helps to distinguish the two phases. In fact, α_I-$Al_{15}(Fe,Mn)_3Si_2$ phase usually lie within ESC particles while the α_{II}-$Al_{15}(Fe,Mn)_3Si_2$ mostly can be seen among the eutectic and has a more polyhedric equiaxial morphology (Fig. 8.b, and *Fig.*). After annealing and T6 heat treatment, the shape and size of that phase did not change (Fig. 9.a, b,c), nor their distribution (Fig. 10). Only slightly blunt corners can be seen for both P and HR alloy after T6 on the larger α_{II}-$Al_{15}(Fe,Mn)_3Si_2$ particles, which may be related to the solution treatment phase.

A small volume fraction of the brittle acicular β-Al_5FeSi phase has been witnessed in the studied samples (Fig. 9d,e,f) for both P and HR alloys. EDS analysis on the β phase was not reported due to technological limitations in analyzing particles of such small size. However, its identification is supported by thermodynamic simulations (Fig. 7) and literature data [16,44,45], which align with the expected appearance of this phase.

The slightly higher content of Fe in HR alloy led to the formation of thicker needle particles in comparison to P alloy (Fig. 10). These results are consistent with the findings of Kucharikova [44], who determined that an AlSi7Mg alloy with 0.655 wt% of Fe exhibited a reduction in β-phases of approximately 12 % compared to the same alloy containing 0.454 wt% of Fe. This variation in size and microstructure was similarly observed by Bosch et al. [13] in a commercial primary AlSi10.5 Mg0.4Fe0.55Mn alloy with a Fe/Mn content comparable to that of the alloy examined in this study.

Bjurenstedt et al. [46] reported that cracked intermetallic compounds are linked to the final fracture, highlighting the critical importance of their distribution. Analyzing the results related to the distribution of Fe-based intermetallic compounds (Fig. 10), it is observed that as Fe content is increased, from P to HR alloy, there is a tendency for the α_{II}-$Al_{15}(Fe,Mn)_3Si_2$ and β-Al_5FeSi particle size and frequency to slightly increase as well. The distribution of the β-Al_5FeSi phase varies depending on the processing conditions. In the as-produced condition (AP), it exhibits an elongated distribution skewed toward higher values, indicative of the presence of elongated lamellae, particularly in the HR alloy, up to 10 μm. A similar value has been found by Fracchia et al. [45] on the HPDC AlSi10MnMg alloy in the as-cast condition. After the heat treatments, the β-Al_5FeSi distribution changes. A slight decrease in the size of the β-Al_5FeSi phase is observed when comparing heat-treated samples to AP components. This may be attributed to a partial dissolution effect, where the lamellar edges round off, and, if fragmented, they take on a more globular appearance rather than elongated shapes (Fig. 9.d,e,f), thereby reducing the typical detrimental effect on the elongation to fracture. According to Narayanan et al. [47], T6 can slightly alter the morphology of needle-like phases, whereas the α-phase that contains Mn remains more stable and resists dissolution. The transition from AP to T6 condition can be tracked through the AN heat treatment, where temperatures are lower than those used for the solution phase of the optimized T6, and therefore some elongated β-Al_5FeSi needles persist, but the distribution begins to shift toward a peak concentrated in diameters of 2–5 μm stage, where the majority of β particles fall after T6.

Table 3
Mn/Fe ratio and SF for the investigated P and HR AlSi10MnMg alloy.

AlSi10MnMg	Fe content [wt%]	Mn content [wt%]	Cr content [wt%]	Mn/Fe ratio [%]	Sludge factor
P	0.127 ± 0.010	0.579 ± 0.024	Not detected	4.6	1.3
HR	0.153 ± 0.005	0.604 ± 0.020	0.005 ± 0.000	3.9	1.4

3.4. Mechanical characterization

3.4.1. Tensile tests

The results of tensile tests on both P and HR alloys in the AP, AN, and T6 conditions are reported in Table 4.

Regarding the strength, the highest yield strength (YS) and ultimate tensile strength (UTS) values were generally recorded in the AP condition for both P and HR alloys. Additionally, it should be noted that the HPDC castings analyzed in this study, in the AP condition, underwent rapid cooling in water at room temperature after extraction from the die, followed by natural aging, which may have contributed from the precipitation of strengthening particles to the observed high value of hardness, YS, and UTS. In particular, the HR specimens showed an average YS 10 MPa higher than the P alloy while maintaining a comparable standard deviation (1 MPa for P alloy and 2 MPa for HR alloy). This difference is likely due to the higher iron and manganese content in HR, present as hard intermetallic compounds, which may slightly enhance the alloy strength. In terms of UTS, the average value is approximately 280 MPa for both P and HR alloys. However, the HR alloy showed a significantly higher standard deviation (21 MPa) compared to the P alloy (4 MPa), likely due to a greater presence of defects and impurities in the HR alloy, mainly Cu, as indicated by the reported chemical analysis (Table 1). The annealing treatment led to a significant reduction in strength. Specifically, about −35 % in YS and UTS for both P and HR alloy. After the T6, the decrease in strength was less pronounced, with reductions of 39 MPa (− 25 %) for P alloy and of 32 MPa (− 20 %) for HR alloy because the coarsening of the microstructure is counterbalanced by precipitation strengthening. However, these findings indicate that T6 treatment, performed at a lower temperature compared to the typical parameters used for low pressure die casting or gravity casting components (usually over 500 °C for 3 or 4 h [48,49]) did not allow the material to achieve the same strength performance as in the AP condition. While the heat treatments caused a significant decrease in tensile resistance (YS and UTS), elongation increased notably after both annealing and T6 for both P and HR alloys. Despite high standard deviation for all the tested samples, elongation improved by at least 40 % following annealing. The improvement in ductility observed after annealing has also been reported by Jarco et al. [50], who demonstrated that a maximum increase in impact strength (KC) of 71 % was achieved for an AlSi11 alloy subjected to soft annealing at 370 °C for 8 h. The most significant increase was achieved with the T6 treatment, which proved to be the best choice for both P and HR alloys in terms of elongation, reaching an average value of 13 % for HR and 16 % for P.

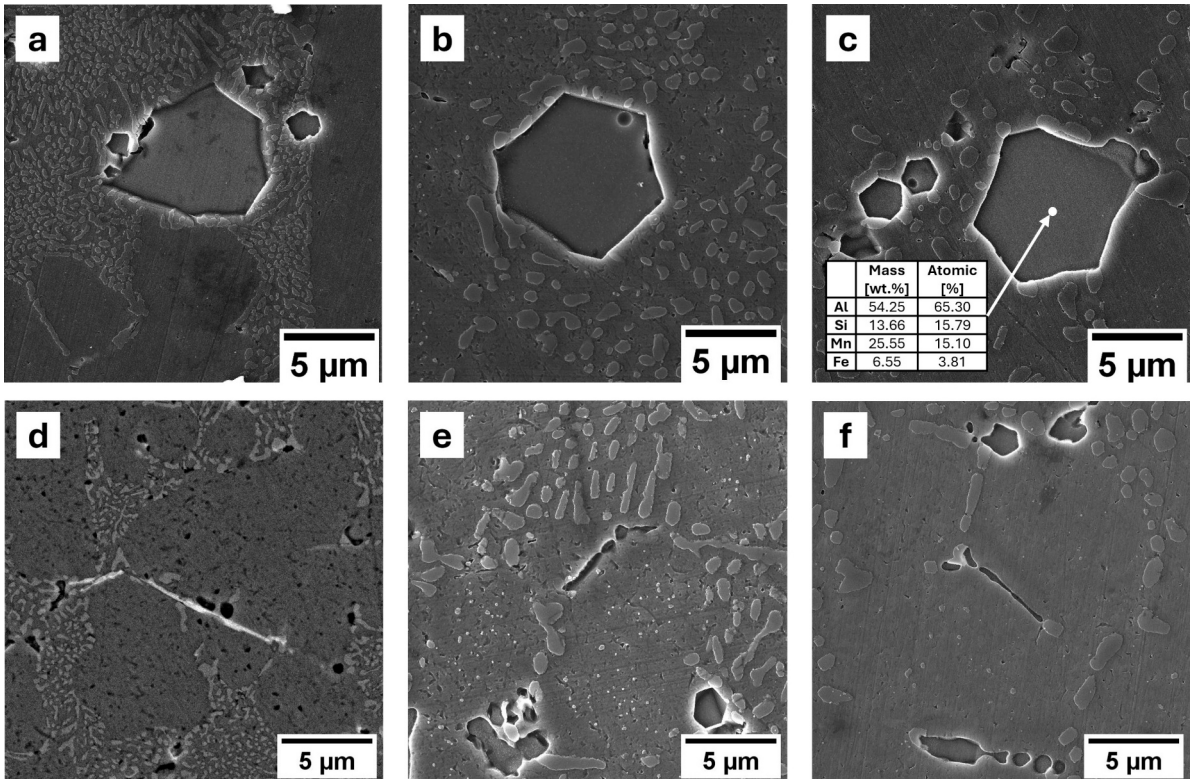

Fig. 9. SEM-FEG Secondary-Electron (a,b,c,e,f) and Back-Scattered (d) images of $\alpha_{I,II}$-$Al_{15}(Fe,Mn)_3Si_2$ (a,b,c) and β-Al5FeSi (d,e,f) intermetallic particles in AlSi10MnMg HR alloy in the AP condition (a,d), after AN (b,e), and following T6 heat treatment (c,f).

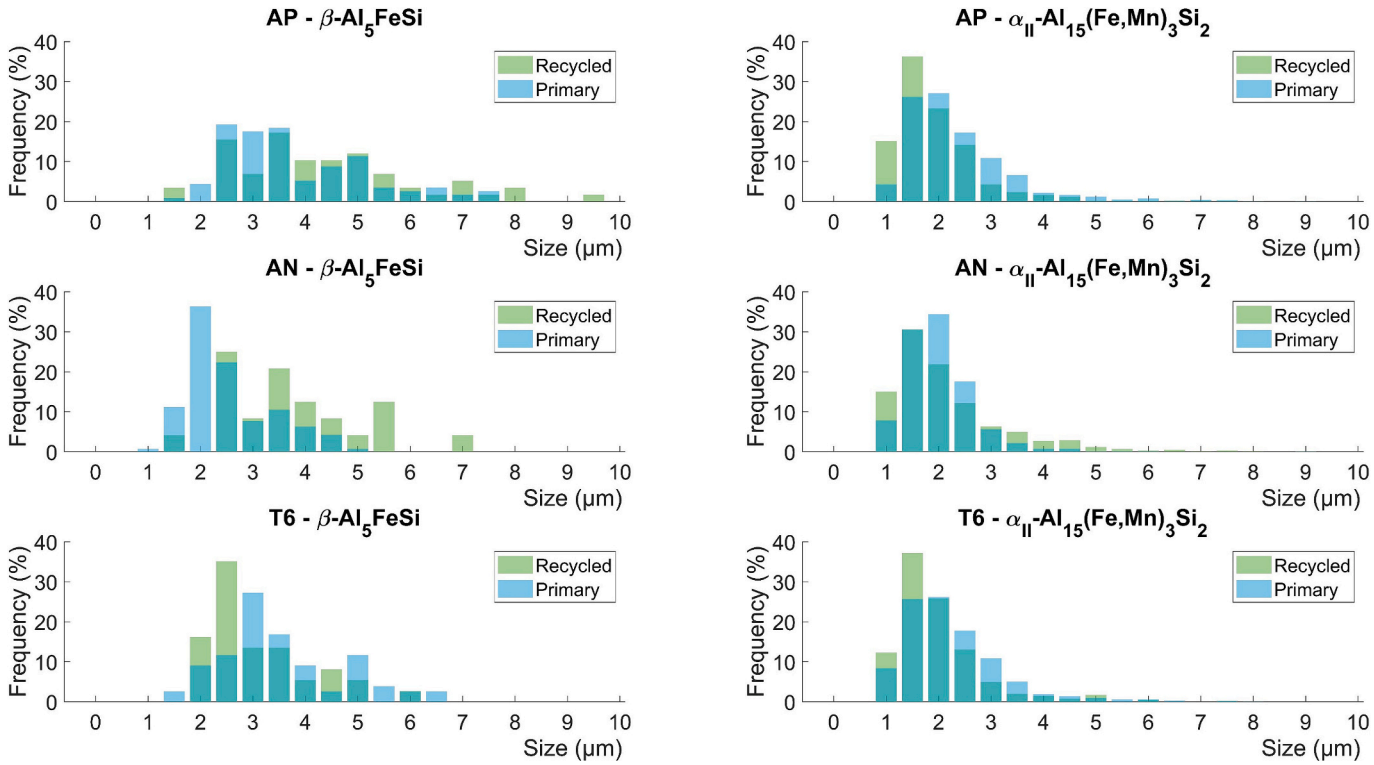

Fig. 10. Iron based Intermetallic phases distribution in AlSi10MnMg alloy in the as-produced condition and after annealing and T6 heat treatments.

This result is significant since, generally, the percentage increase in e_f % is the main reason why heat treatments are proposed for HPDC alloys. Nicklas et al. [51], on 2 mm thick primary AlSi10MnMg(Fe) with 0.17 % Fe samples, reported a UTS of 251 MPa in the as-cast condition, with an elongation of 3.67 %. After T6 heat treatment, the UTS increased to 327 MPa, with an elongation of 6.90 %. The values found in this study after

Table 4
Mechanical properties of the P and HR AlSi10MnMg alloy under different conditions: hardness, yield strength (YS), ultimate tensile strength (UTS) and elongation (e_f %).

Alloy	Condition	Hardness		YS		UTS		e_f %	
		[HBW 2.5/62.5]		[MPa]		[MPa]		[%]	
		avg	st dev	avg	st dev	avg	st dev	avg	st dev
P	AP	86.7	1.9	146	1	280	4	7.5	3.8
	AN	56.4	1.5	92	4	181	6	10.6	2.4
	T6	66.7	0.9	118	3	210	3	16.6	2.6
HR	AP	86.8	1.0	157	2	280	21	7.1	3.8
	AN	57.7	1.1	97	3	182	5	10.8	1.5
	T6	65.7	1.4	125	5	210	1	13.3	2.9

T6 show higher elongation and lower UTS, likely due to the lower solution treatment temperature and shorter duration used (Nicklas et al. [51] reported 490 °C for 3 h as solution heat treatment parameters), which may have resulted in a smaller volume fraction of strengthening precipitates.

To provide a comprehensive overview of the results, an Ashby map (Fig. 11) was constructed with elongation (%strain) on the x-axis and tensile strength on the y-axis. This map includes the data obtained in this study for P and HR alloys in AP, AN, and T6 conditions, alongside literature data on similar HPDC alloys and commercial HPDC aluminum casting alloys. The shape of the plotted markers indicates the variation range of each property, with more elongated ellipses representing a higher standard deviation. The purple ellipses are cast alloys, the red ones are HPDC alloys, and the orange ellipses are AlSi7 alloys. In terms of tensile strength, the as-produced alloys investigated in the present study (blue for primary, green for high recycled content in Fig. 11) have higher values compared to the heat-treated ones and are equivalent to the AlSi17Cu4 (A390) alloy and the T6 heat treated AlSi7Mg (A356, EN AC 42000) produced by permanent mold cast. The experimental results also align well with the results presented by Niklas et al. [51], who investigated primary and highly recycled AlSi10MnMg (EN AC 43500) alloy. Interestingly, the T6 heat treated HR alloy by Niklas et al. [51] overlaps with the as-produced alloys of the present study, likely due to the natural aging induced by the rapid cooling of the casting after extraction from the die. From the environmental impact perspective, the T6 heat treatment presents an extra step of energy consumption and CO_2 emissions compared with the AP; the similar mechanical performance of as-produced alloys suggests the possibility for environmental savings.

A similar comment is valid when looking at elongation to failure, comparing the as-produced alloys with the results by Niklas et al. [51]. The best performing alloys are the T6 heat treated ones, at expense of tensile strength, and they are outstanding candidates in the overall family of cast alloys. The AlSi7Mg alloys produced by HPDC [52] are partially overlapping with the HR alloy of the present study.

3.4.2. *Fractographic characterization*

Observation of fracture surfaces in HPDC aluminum alloys can provide valuable insights into the fracture mechanisms and the factors

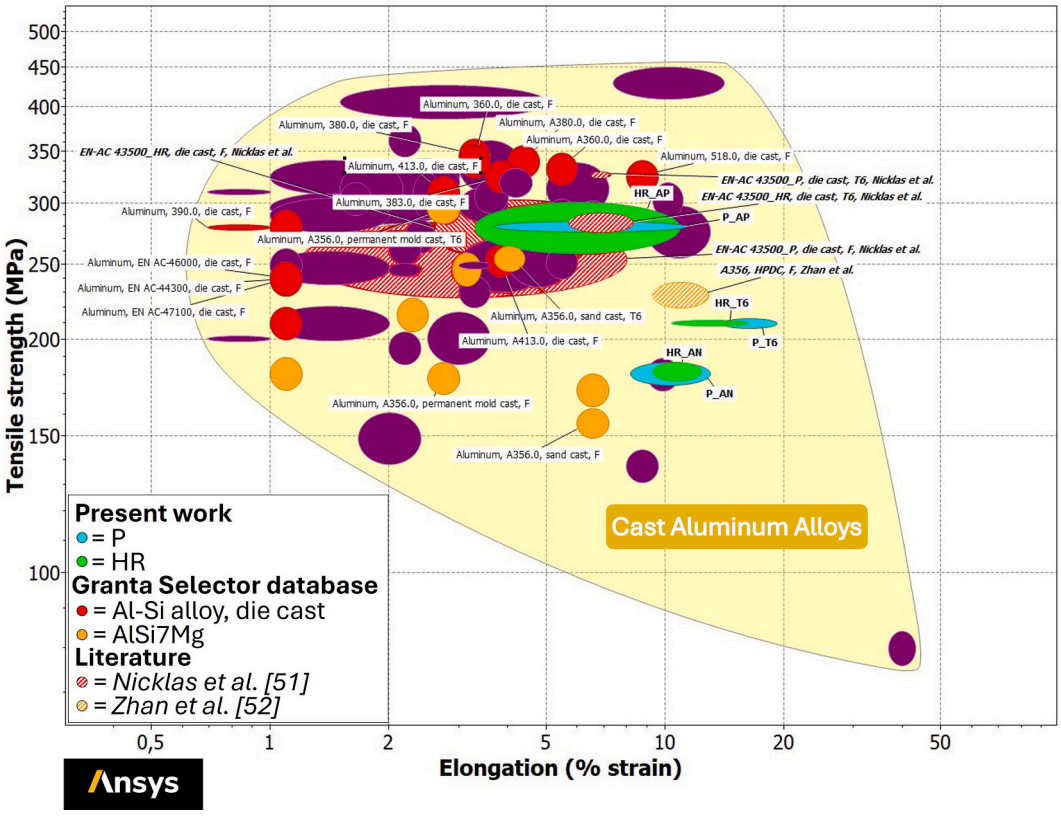

Fig. 11. Comparison of UTS and elongation to failure (ε_f %) of studied P and HR AlSi10MnMg alloy under different conditions (AP, AN, T6) with literature data in Ashby Map.

influencing the material ductility. The P and HR alloys in AP condition exhibited similar behavior governed by a quasi-cleavage fracture mode (Fig. 12). In fact, sub-micrometric dimples and tear ridges were present in the core of the tested samples, surrounded by small cleavage planes and fractured intermetallic compounds (Fig. 12.a,b). Specifically, the morphology of the intermetallics aids in recognizing their presence and identifying them, as in the case of the one shown in Fig. 12b, which is likely an α-$Al_{15}(Fe,Mn)_3Si_2$. Its chemical composition is therefore expected to be similar to that presented in Fig. 9c. The small and flat dimples are generated by the fine microstructure associated with the HPDC process, which limits pore growth and eutectic silicon particles size. Heat treatment can significantly alter the fracture behavior of both primary and high recycled content alloy. Liu et al. [53] indicated a transition from brittle to ductile fracture on an Al10Si0.5Mn0.3 Mg T7 (solution, quenching, and overaging) heat treated. This transformation is primarily attributed to the spheroidization and fragmentation of the eutectic Si particles during the heat treatment process. Also, in this study, it has been observed that after annealing and T6, the fracture behavior becomes completely ductile, with numerous bigger and elongated dimples on the fracture surfaces (Fig. 12.c-f). No evidence of cleavage planes is visible in Fig. 12.c-f.

Characterizing the fracture surface can reveal the role of various microstructural features in the fracture process. Large Fe-based intermetallic compounds and large pores may become potential sites for crack initiation or propagation as evidenced by their presence on the fracture surfaces (Fig. 13.a,b,d). The cracking of a polygonal α_I-$Al_{15}(Fe,Mn)_3Si_2$ phase (~10 μm) in the AP fracture surface of HR alloy is shown in Fig. 13.b.

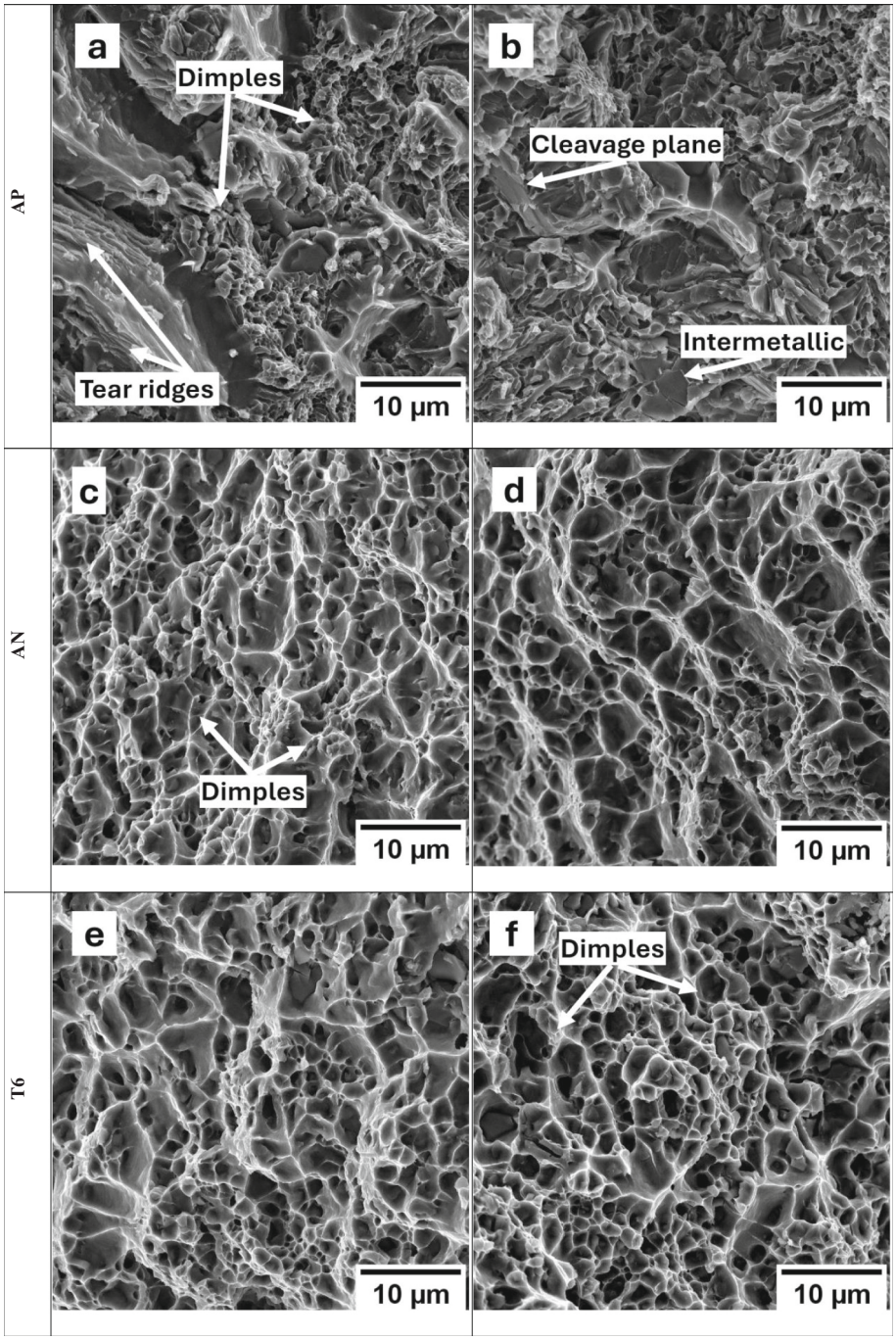

Fig. 12. Longitudinal section of the fracture surface relative to (a,c,e) P and (b,d,f) HR AlSi10MnMg alloy in the (a-b) AP, (c-d) AN and (e-f) T6 conditions.

Niklas et al. [26] suggested that casting defects (such as pores, shrinkages, cold shots, and cold flakes) are major contributors to the substantial reduction in elongation observed in the AlSi10MnMg(Fe) alloy. Fracture tends to initiate at the location of the largest pore within the gauge section and as the size of the largest pore increases, the elongation to fracture decreases [53]. This suggests that, while the heat treatment spheroidizes the eutectic Si and improves ductility, the slightly increase in defect area fraction (Fig. 4.b) associated with the exposure to solution heat treatment and annealing may worsen the final elongation to fracture, particularly evident in the AN condition for both P and HR. Another feature to consider is the presence of ESCs. These feeding failures are susceptible to intergranular fracture because the weak bonding between ESC and the matrix promotes the crack propagation along the ESC boundaries and other porosities, resulting in a tortuous crack path (Fig. 13.c). However, when the stresses are high enough, also trans-granular fracture could arise from ESC leading to a flatter crack route [53].

Examples of the microcracks nucleation around defects, such as the shrinkage pore edge and further propagate along the boundary of the dendrites, ESC, fractured eutectic silicon particles and large Fe-based intermetallic are reported on Fig. 14.

3.5. Environmental impact assessment

The environmental impact assessment is a powerful tool that, by taking as input the energy required for each step of the process, can provide a comprehensive view of the contributions to overall energy consumption and CO_2 emissions. The results, presented in Fig. 15, highlight the differences in environmental impact between primary and recycled AlSi10MnMg in the as-produced (AP) condition and illustrate how heat treatments, annealing (AN), and T6, modify this impact in the recycled alloy. An important finding is that recycled material requires significantly less energy than primary production, though this reduction is not as high as 95 % when considering primary aluminum produced in Europe, where energy consumption is lower than the global average [6,8].

Once the material is cast into a shock-tower, the manufacturing contribution is shown in the next group of columns on the right (in the graphs in Fig. 15). These columns illustrate the impact of casting, cutting and trimming operations, as well as the impact of heat treatment on energy consumption (Fig. 15.a) and carbon footprint (Fig. 15.b). While the AP condition shows that manufacturing has a negligible impact compared to the material itself, applying a heat treatment increases the environmental burden, particularly with T6, which includes a high-temperature solution phase. The use of a secondary alloy determines an overall decrease of 28 % in energy use and 31 % of CO_2 footprint during the component life. Similar values are maintained, in the 27–28 % and 29–30 % ranges for energy and CO_2 footprint, respectively, when applying the annealing and T6 heat treatments.

Finally, in Fig. 15, additional phases show comparable contributions across all primary and recycled alloy conditions. These include the component transportation, which has a minimal impact under the assumption that distribution is limited to Europe, and the use phase, which considers the expected lifespan of the component in an

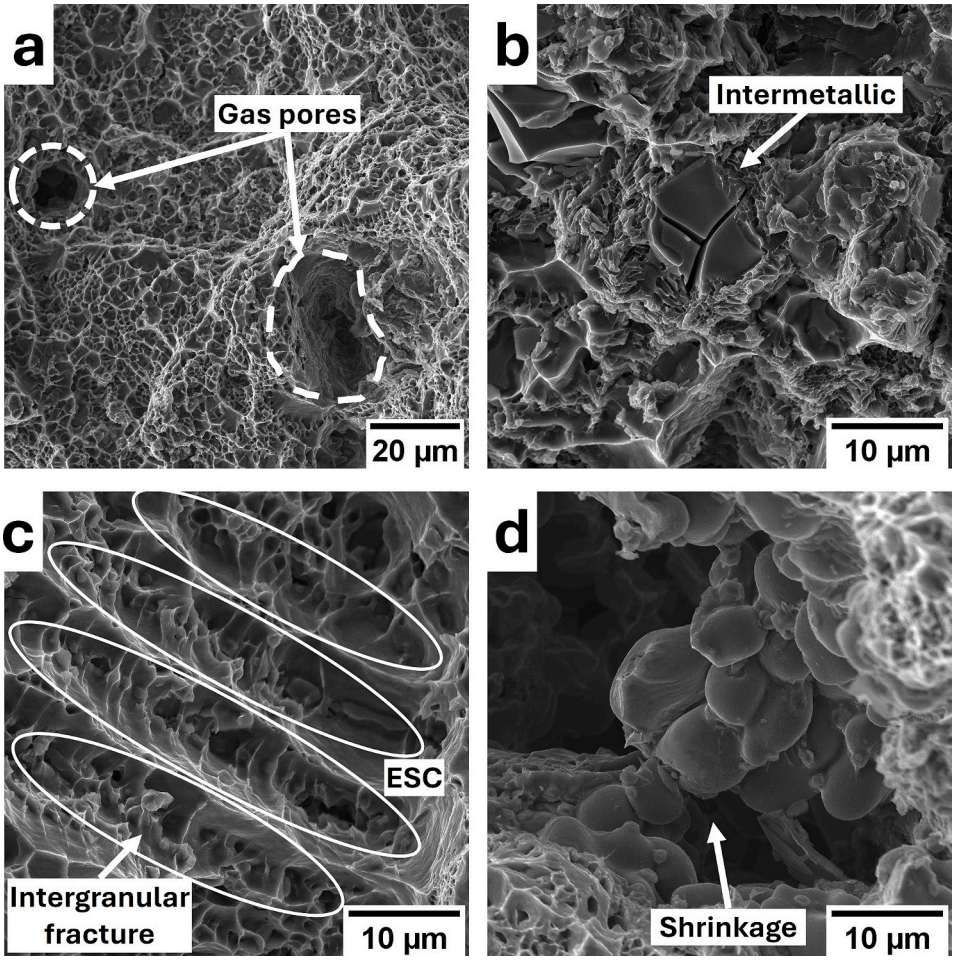

Fig. 13. SEM-FEG micrographs of fractographic surface features on AlSi10MnMg alloy: (a) Gas pores, (b) intermetallic, (c) ESC trace, (d) shrinkage. The images were taken from HR alloy in (b) AP and (c) T6 conditions, and from P alloy in (a, d) AN condition.

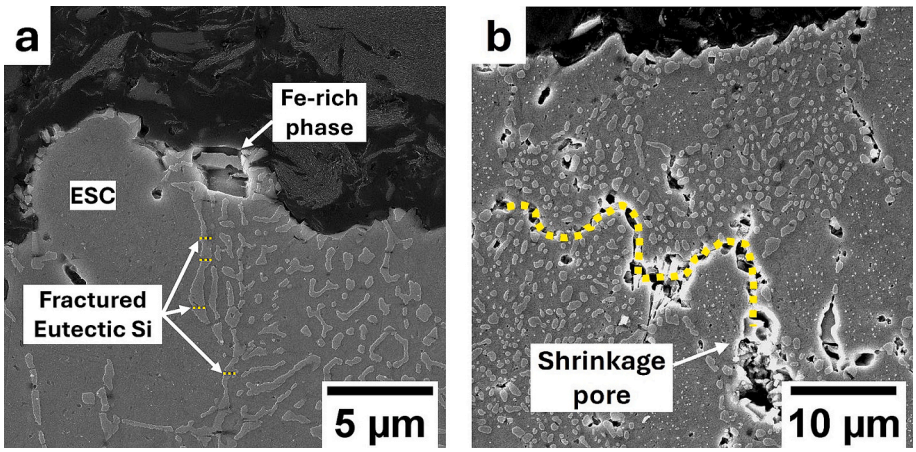

Fig. 14. SEM-FEG micrograph of fractographic surface crack propagation along: (a) ESC, Fe-rich phase and fractured eutectic silicon particles; (b) shrinkage. The images were taken from HR alloy in (a) AP and (b) AN conditions.

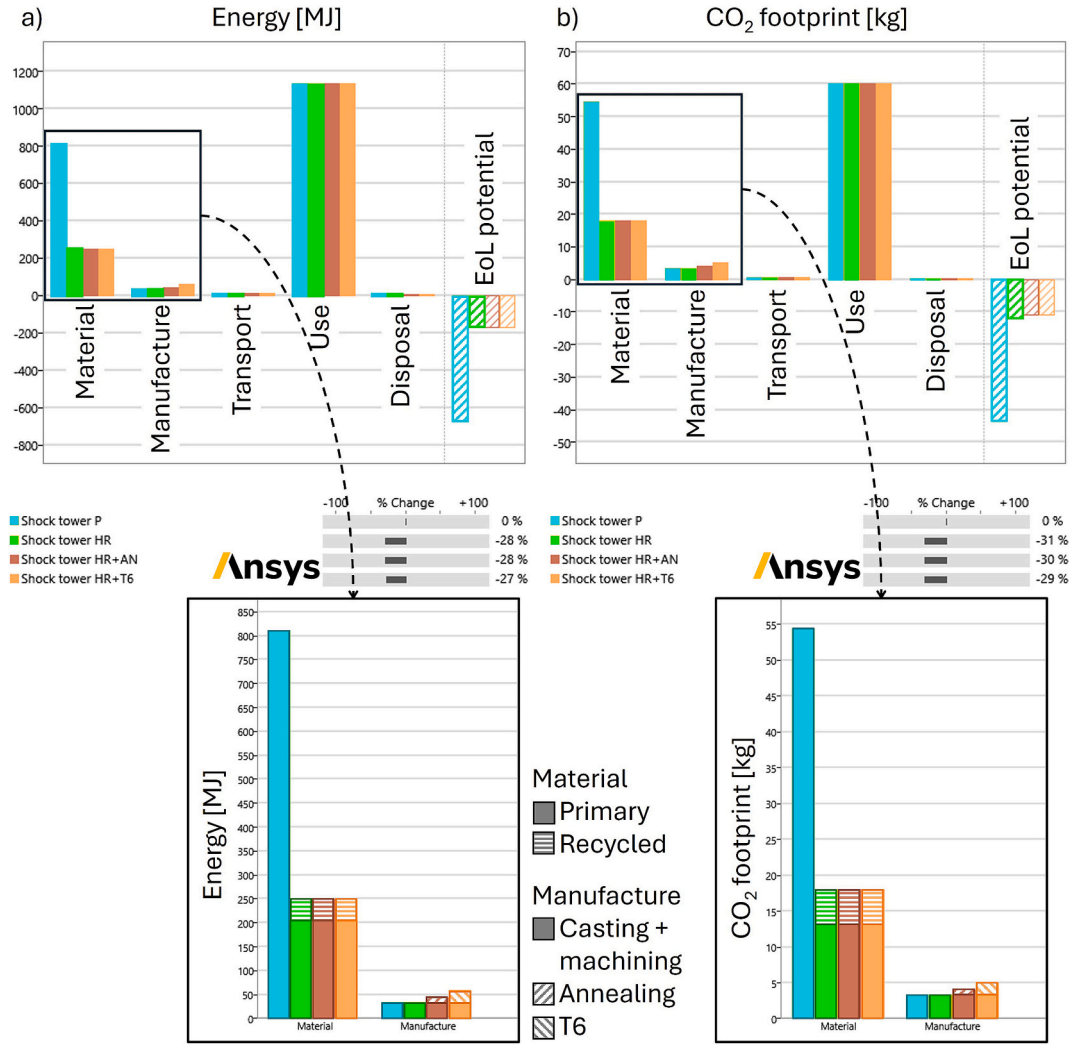

Fig. 15. Eco Audit of shock tower: a) energy; b) CO_2 footprint.

automotive application. Further studies focusing on the durability of the component, particularly on corrosion and wear behavior, could provide more details and refine the evaluation of the use phase. The disposal and End-of-Life (EoL) potential highlight how the material can be collected and reutilized even after its service life.

Looking to future developments and strategies for a continuous decrease in the environmental impact of aluminum alloys, an effective action would be to prefer, when possible, no high temperature heat treatments and alloys with lower Si contents. Si carries a significant heat of fusion, and it is often required as an extra addition to scrap aluminum

in order to meet the composition range of near-eutectic cast aluminum alloys. From a performance point of view, an example is the AlSi7Mg alloy produced by HPDC that is comparable in elongation to the heat-treated AlSi10MnMg alloy in Fig. 11. On the other hand, the melting and handling of low-Si alloys require a higher melting and holding temperatures, e.g. from a foundry practice perspective the pouring temperature is around ~680 °C for an AlSi10 alloy and around ~720 °C for an AlSi7 alloy. Higher temperature in the furnaces leads to higher energy consumption and an indirect CO_2 footprint, as well as a decreasing die life. A careful evaluation would be needed from case to case to find the best solution, compromising between performance and environmental impact.

4. Conclusions

The following key conclusion can be drawn from the characterization of samples extracted from two shock towers manufactured by HPDC using primary (P) and high-recycled content (HR) AlSi10MnMg alloy, respectively, and studied in as-produced (AP) condition (natural aging that follows the rapid quenching after the HPDC), annealing (AN) and T6 heat treatments:

a. The similar chemical composition of P and HR AlSi10MnMg alloy led to comparable microstructures in the AP condition with fine and elongated eutectic Si particles, small and compact polyhedral α-$Al_{15}(Fe,Mn)_3Si_2$ and few β-Al_5FeSi acicular intermetallic compounds.
b. AN and T6 heat treatments resulted in eutectic Si fragmentation, spheroidization, coarsening, and an increase in interparticle spacing for both P and HR alloys. A negligible effect of heat treatment was observed on SDAS, defects, and Fe-based intermetallic compounds.
c. For both the P and HR alloys, AP specimens showed the highest strength and lowest ductility. AN led to the greatest ductility, while the T6 treatment led to a trade-off between strength and elongation.
d. The fractographic characterization confirmed for both P and HR alloys the results of mechanical tests, by showing areas of quasi-cleavage on fracture surfaces for the AP specimens and the presence of ductile dimples for both the AN and T6 specimens.
e. Using recycled alloy significantly reduces environmental impact, requiring only about 1/4 of the energy and CO_2 emissions compared to primary alloy production. However, applying heat treatments increases energy consumption, with T6 adding +30 % and AN +25 % impact on the overall component life. Therefore, heat treatment should be applied only when necessary to meet specific strength, although lower than AP, and ductility requirements, as the AP condition offers a good balance between performance and sustainability.

CRediT authorship contribution statement

Riccardo Arcaleni: Writing – review & editing, Writing – original draft, Methodology, Investigation, Data curation. **Luca Girelli:** Writing – review & editing, Writing – original draft, Methodology, Conceptualization, Data curation. **Lavinia Tonelli:** Methodology, Conceptualization, Writing – review & editing. **Lucia Lattanzi:** Writing – review & editing, Methodology, Conceptualization. **Marialaura Tocci:** Validation, Supervision, Conceptualization. **Alessandro Morri:** Validation, Supervision, Conceptualization. **Annalisa Pola:** Validation, Supervision, Conceptualization. **Lorella Ceschini:** Validation, Supervision, Conceptualization.

Funding

Financed by the European Union - NextGenerationEU (National Sustainable Mobility Center CN00000023, Italian Ministry of University and Research Decree n. 1033–17/06/2022, Spoke 11 - Innovative Materials & Lightweighting). The opinions expressed are those of the authors only and should not be considered as representative of the European Union or the European Commission's official position. Neither the European Union nor the European Commission can be held responsible for them.

Declaration of competing interest

The authors declare that they do not have any financial or personal relationships with other people or organizations that could have inappropriately influenced this study.

Acknowledgements

The Authors would like to acknowledge C. Rivadossi of Raffmetal S. p.A. (Casto, BS, Italy) for the support in melting of the alloys for the chemical composition analysis, M. Falconi of University of Brescia - Department of Mechanical and Industrial Engineering (Brescia, BS; Italy) for the support in the T6 treatment optimization and both C. Cascioli and T. Salvador of the University of Bologna - Department of Industrial Engineering (Bologna, BO, Italy) for the energy consumption measurements. Ansys is gratefully acknowledged for providing Granta Selector software through the Research Partnership with Tekniska Högskolan i Jönköping.

Appendix A

Table A1
Data used for environmental impact evaluation in Granta Software Eco Audit tool

Parameter	Data	Note/Reference
Material	AlSi10MnMg P AlSi10MnMg HR	
Recycled Content	P (0 %) Embodied energy: 160–200 MJ/kg CO_2 footprint: 11–13 kg/kg HR (75 %) Embodied energy recycling: 10–15 MJ/kg CO_2 footprint recycling: 0.6–2.35 kg/kg	EPD-IES-0006063:002 [34] https://environdec.com/library/epd6063
Part mass	4.5 kg	https://www.gfcs.com/en/market-segments/light-vehicles/shock-tower0.html
Primary process	Casting Energy: 5.8–8 MJ/kg CO_2 footprint: 0.5–0.8 kg/kg	EPD-IES-0006063:002 [34] https://environdec.com/library/epd6063

(*continued on next page*)

Table A1 (*continued*)

Parameter	Data	Note/Reference
Secondary process	Cutting, trimming, and machining	
Removed material	10 %	
Manufacture		
Casting	Energy: 5.8–8 MJ/kg CO_2 footprint: 0.5–0.8 kg/kg	Granta Selector database
Heat treatment	Annealing (AN) Energy: 0.7–2.9 MJ/kg CO_2 footprint: 0.1–0.2 kg/kg T6 Energy: 2–7.5 MJ/kg CO_2 footprint: 0.2–0.6 kg/kg	Measured in a furnace on 1 kg and 4.5 kg samples (graph in Fig. A1). A cold ingot was inserted in a cold furnace
Transport	Transport type: Truck >32 t, EURO 6, Distance: 1200 km	Granta Selector database
Use	Fuel: Hybrid gasoline Mobility type: electric family car Area of use: The whole world Product life: 15 years Usage: 300 day/year Distance: 40 km/day	Granta Selector database
Disposal	Recycle Recovered: 90 %	

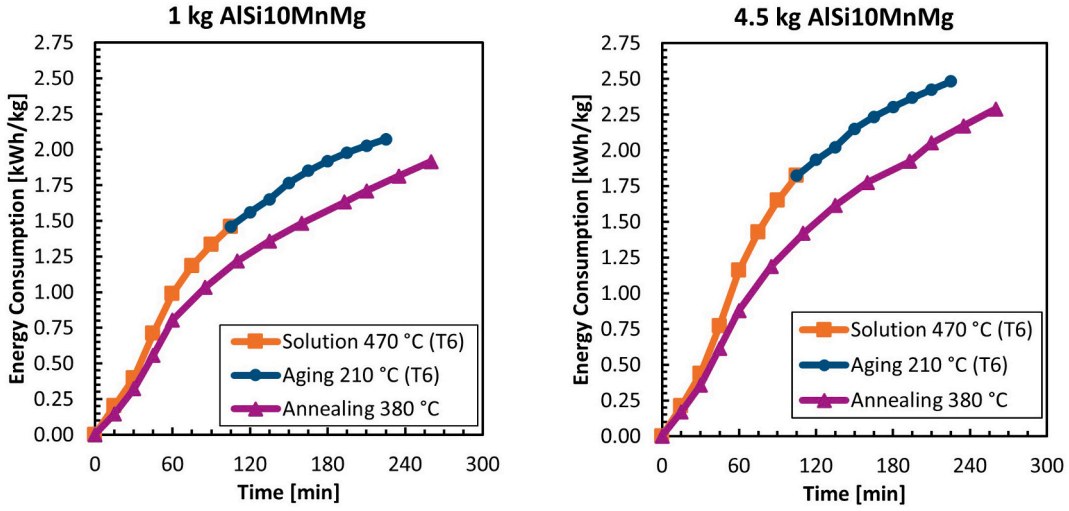

Fig. A1. Energy consumption measured during different heat treatment conditions for (a) 1 kg and (b) 4.5 kg of AlSi10MnMg alloy.

Data availability

Data will be made available on request.

References

[1] D. Lehmhus, Advances in metal casting technology: a review of state of the art, challenges and trends—part I: changing markets, changing products, Metals 12 (11) (2022) 1959, https://doi.org/10.3390/met12111959.

[2] K. Wärmefjord, J. Hansen, R. Söderberg, Challenges in geometry assurance of megacasting in the automotive industry, J. Comput. Inf. Sci. Eng. 23 (6) (2023) 060801, https://doi.org/10.1115/1.4062269.

[3] "TESLA, 2022, 'INTEGRATED ENERGY ABSORBING CASTINGS, PCT/ US2021/044780,' https://patentscope.wipo.int/search/en/detail.jsf?docId=WO2022031991".

[4] F. Niklas, New addressable applications for Rheocasting to escape from an oversupplied market, SSP 348 (2023) 61–67, https://doi.org/10.4028/p-K3Dfyn.

[5] Z. Niu, G. Liu, T. Li, S. Ji, Effect of high pressure die casting on the castability, defects and mechanical properties of aluminium alloys in extra-large thin-wall castings, J. Mater. Process. Technol. 303 (2022) 117525, https://doi.org/10.1016/j.jmatprotec.2022.117525.

[6] T. Peng, L. Ren, E. Du, X. Ou, X. Yan, Life cycle energy consumption and greenhouse gas emissions analysis of primary and recycled Aluminum in China, Processes 10 (11) (2022) 2299, https://doi.org/10.3390/pr10112299.

[7] D. Raabe, The materials science behind sustainable metals and alloys, Chem. Rev. 123 (5) (2023) 2436–2608, https://doi.org/10.1021/acs.chemrev.2c00799.

[8] D. Raabe, et al., Making sustainable aluminum by recycling scrap: the science of 'dirty' alloys, Prog. Mater. Sci. 128 (2022) 100947, https://doi.org/10.1016/j.pmatsci.2022.100947.

[9] J. Cui, H.J. Roven, Recycling of automotive aluminum, Trans. Nonferrous Metals Soc. China 20 (11) (2010) 2057–2063, https://doi.org/10.1016/S1003-6326(09)60417-9.

[10] J.M. Cullen, J.M. Allwood, Mapping the global flow of Aluminum: from liquid Aluminum to end-use goods, Environ. Sci. Technol. 47 (7) (2013) 3057–3064, https://doi.org/10.1021/es304256s.

[11] Silicon, Granta Selector 2023 R1, Version 23.1.1, 2025.

[12] EN 1706:2020, Aluminium and aluminium alloys. Castings. Chemical composition and mechanical properties Table 1 - Chemical composition of aluminium castings, BSI Standards Publication, 2020.

[13] D. Bösch, et al., Secondary Al-Si-mg high-pressure die casting alloys with enhanced ductility, Metall. Mater. Trans. A 46 (3) (2015) 1035–1045, https://doi.org/10.1007/s11661-014-2700-8.

[14] N. Balasubramani, M. Moodispaw, A.A. Luo, Controlling the Fe-intermetallic phases and mechanical properties of secondary Al-9Si-1Fe alloy with Cr and Mn additions, J. Mater. Sci. Technol. 206 (2025) 135–152, https://doi.org/10.1016/j.jmst.2024.04.014.

[15] L. Ceschini, I. Boromei, A. Morri, S. Seifeddine, I.L. Svensson, Effect of Fe content and microstructural features on the tensile and fatigue properties of the Al–Si10–Cu2 alloy, Mater. Des. 1980-2015 (36) (2012) 522–528, https://doi.org/10.1016/j.matdes.2011.11.047.

[16] M.A. Moustafa, Effect of iron content on the formation of β-Al5FeSi and porosity in Al–Si eutectic alloys, J. Mater. Process. Technol. 209 (1) (2009) 605–610, https://doi.org/10.1016/j.jmatprotec.2008.02.073.

[17] L. Ceschini, A. Morri, S. Toschi, A. Bjurenstedt, S. Seifeddine, Influence of sludge particles on the fatigue behavior of Al-Si-cu secondary aluminium casting alloys, Metals 8 (4) (2018) 268, https://doi.org/10.3390/met8040268.

[18] J. Gobrecht., Schwereseigrungen von Eisen, Mangan und Chrom in Aluminium-Silicum-Gußlegierungen (Teil 1), Giesserei 61 (1975) 263–265.
[19] J. Jorstad, Understanding sludge, Die Cast. Eng. 30 (1986) 30–36.
[20] J.M. Sanchez, M. Arribas, H. Galarraga, M. Garcia de Cortazar, M. Ellero, F. Girot, Effects of Mn addittion, cooling rate and holding temperature on the modification and purification of iron-rich compounds in AlSi10MnMg(Fe) alloy, Heliyon 9 (2) (2023) e13005, https://doi.org/10.1016/j.heliyon.2023.e13005.
[21] E. Cinkilic, M. Moodispaw, J. Zhang, J. Miao, A.A. Luo, A new recycled Al–Si–mg alloy for sustainable structural die casting applications, Metall Mater Trans A 53 (8) (2022) 2861–2873, https://doi.org/10.1007/s11661-022-06711-4.
[22] A. Niklas, S. Orden, A. Bakedano, M. da Silva, E. Nogués, A.I. Fernández-Calvo, Effect of solution heat treatment on gas porosity and mechanical properties in a die cast step test part manufactured with a new AlSi10MnMg(Fe) secondary alloy, Mater. Sci. Eng. A 667 (2016) 376–382, https://doi.org/10.1016/j.msea.2016.05.024.
[23] X.Y. Jiao, et al., The microstructure characteristics and fracture behavior of the polyhedral primary iron-rich phase and plate-shaped eutectic iron-rich phase in a high-pressure die-cast AlSi10MnMg alloy, J. Mater. Sci. Technol. 140 (2023) 201–209, https://doi.org/10.1016/j.jmst.2022.09.014.
[24] V. Rauta, C. Cingi, J. Orkas, Effect of annealing and metallurgical treatments on thermal conductivity of aluminium alloys, Inter Metalcast 10 (2) (2016) 157–171, https://doi.org/10.1007/s40962-015-0017-z.
[25] X.G. Hu, et al., Blistering in semi-solid die casting of aluminium alloys and its avoidance, Acta Mater. 124 (2017) 446–455, https://doi.org/10.1016/j.actamat.2016.11.032.
[26] B. Dybowski, A. Kiełbus, Ł. Poloczek, Effects of die-casting defects on the blister formation in high-pressure die-casting aluminum structural components, Eng. Fail. Anal. 150 (2023) 107223, https://doi.org/10.1016/j.engfailanal.2023.107223.
[27] R. Gomes, et al., Development of heat treatments for structural parts in aluminium alloys produced by high-pressure die casting (HPDC), Metals 14 (9) (2024) 1059, https://doi.org/10.3390/met14091059.
[28] "RHEINFELDEN ALLOYS GmbH & Co. KG, 'Silafont®-36 [AlSi10MnMg] – Processing Data Sheet,' in Aluminium Casting Alloys Handbook: Processing Data Sheets, Version 8, 2015. [Online]. Available: https://rheinfelden-alloys.eu/wp-content/uploads/2015/07/05-Silafont-Processing.pdf.
[29] "Raffmetal S.P.A., 'EN 43500 AlSi10MnMg – Technical Data Sheet,' in Aluminium Alloys – Processing Data Sheets, Version 2020. [Online]. Available: https://www.raffmetal.com/it/prodotti/leghe-al-silicio/al-sil10mnmg/.
[30] International Organization for Standardization: ISO 14707:2015, Surface Chemical Analysis—Glow Discharge Opti cal Emission Spectrometry (GD-OES), Introduction to Use, International Organization for Standardization, Geneva, Switzerland, 2015.
[31] R.N. Lumley, R.G. O'Donnell, D.R. Gunasegaram, M. Givord, Heat treatment of high-pressure die castings, Metall Mater Trans A 38 (10) (2007) 2564–2574, https://doi.org/10.1007/s11661-007-9285-4.
[32] Abramoff, M.D., Magalhaes, P.J., Ram, S.J., Image processing with ImageJ, Biophoton. Int. 11 (7) (2004) 36–42.
[33] J.O. Andersson, T. Helander, L. Höglund, P.F. Shi, B. Sundman, Thermo-calc and DICTRA, computational tools for materials science, Calphad 26 (2002) 273–312.
[34] G. Di Egidio, L. Ceschini, A. Morri, C. Martini, M. Merlin, A novel T6 rapid heat treatment for AlSi10Mg alloy produced by laser-based powder bed fusion: comparison with T5 and conventional T6 heat treatments, Metall. Mater. Trans. B Process Metall. Mater. Process. Sci. 53 (1) (2022) 284–303, https://doi.org/10.1007/s11663-021-02365-6.
[35] X.Y. Jiao, et al., Characterization of externally solidified crystals in a high-pressure die-cast AlSi10MnMg alloy and their effect on porosities and mechanical properties, J. Mater. Process. Technol. 298 (2021) 117299, https://doi.org/10.1016/j.jmatprotec.2021.117299.
[36] J. Campbell, Entrainment defects, Mater. Sci. Technol. 22 (2) (2006) 127–145, https://doi.org/10.1179/174328406X74248.
[37] M.R.S. Ganesh, N. Reghunath, M.J. Levin, A. Prasad, S. Doondi, K.V. Shankar, Strontium in Al–Si–mg alloy: a review, Met. Mater. Int. 28 (1) (2022) 1–40, https://doi.org/10.1007/s12540-021-01054-y.
[38] Y.C. Lin, S.-C. Luo, J. Huang, L.-X. Yin, X.-Y. Jiang, Effects of solution treatment on microstructures and micro-hardness of a Sr-modified Al-Si-mg alloy, Mater. Sci. Eng. A 725 (2018) 530–540, https://doi.org/10.1016/j.msea.2018.04.049.
[39] V. Pa'ramo, R. Colás, E. Velasco, S. Valtierra, Spheroidization of the Al-Si eutectic in a cast Aluminum alloy, J. Mater. Eng. Perform. 9 (6) (2000) 616–622, https://doi.org/10.1361/105994900770345467.
[40] K. Lee, Y.N. Kwon, S. Lee, Effects of eutectic silicon particles on tensile properties and fracture toughness of A356 aluminum alloys fabricated by low-pressure-casting, casting-forging, and squeeze-casting processes, J. Alloys Compd. 461 (1–2) (2008) 532–541, https://doi.org/10.1016/j.jallcom.2007.07.038.
[41] J. Santos, Al-7Si-mg Semi-Solid Castings: Microstructure and Mechanical Properties, Jönköping University, Jönköping, Sweden, 2018.
[42] A. Bongiovanni, M.D. Silva, A. Castellero, Comparison of as Cast and T6 Heat Treatment on High End-of-Life-Scrap Secondary Aluminium Alloy for High-Pressure Die Casting Automotive Structural Components, 2024.
[43] X. Wang, H. Zhao, Q. Xu, Z. Han, Clustering characteristics of Fe-rich intermetallics in high vacuum die cast AlSiMgMn alloys with high resolution μ-CT inspection, Mater. Charact. 207 (2024) 113607, https://doi.org/10.1016/j.matchar.2023.113607.
[44] L. Kuchariková, et al., The Effect of the β-Al5FeSi Phases on Microstructure, Mechanical and Fatigue Properties in A356.0 Cast Alloys with Higher Fe Content without Additional Alloying of Mn, Materials 14 (8) (2021) 1943, https://doi.org/10.3390/ma14081943.
[45] E. Fracchia, F.S. Gobber, M. Rosso, Effect of alloying elements on the Sr modification of Al-Si cast alloys, Metals 11 (2) (2021) 342, https://doi.org/10.3390/met11020342.
[46] A. Bjurenstedt, E. Ghassemali, S. Seifeddine, A.K. Dahle, The effect of Fe-rich intermetallics on crack initiation in cast aluminium: an in-situ tensile study, Mater. Sci. Eng. A 756 (2019) 502–507, https://doi.org/10.1016/j.msea.2018.07.044.
[47] L.A. Narayanan, F.H. Samuel, J.E. Gruzleski, Dissolution of iron intermetallics in Al-Si alloys through nonequilibrium heat treatment, Metall Mater Trans A 26 (8) (1995) 2161–2174, https://doi.org/10.1007/bf02670687.
[48] ASTM Standard B917/B917M-2001, Standard Practice for Heat Treatment of Aluminum-Alloy Castings from All Processes, ASTM International, West Conshohocken, PA, USA, 2001.
[49] J. Pezda, Optimization of heat treatment parameters of AlSi7Mg alloy, Materials 15 (3) (2022) 1163, https://doi.org/10.3390/ma15031163.
[50] A. Jarco, Effect of soft annealing treatment on impact strength and hardness of the EN AC-AlSi11 alloy, Arch. Foundry Eng. 17 (3) (2017) 55–58, https://doi.org/10.1515/afe-2017-0090.
[51] A. Niklas, A. Bakedano, S. Orden, M. da Silva, E. Nogués, A.I. Fernández-Calvo, Effect of microstructure and casting defects on the mechanical properties of secondary AlSi10MnMg(Fe) test parts manufactured by vacuum assisted high pressure die casting technology, Mater. Today Proc. 2 (10) (2015) 4931–4938, https://doi.org/10.1016/j.matpr.2015.10.059.
[52] H. Zhan, et al., Unified casting (UniCast) aluminum alloy—a sustainable and low-carbon materials solution for vehicle lightweighting, J. Mater. Sci. Technol. 154 (2023) 251–268, https://doi.org/10.1016/j.jmst.2023.02.003.
[53] R. Liu, et al., Influence of pore characteristics and eutectic particles on the tensile properties of Al–Si–Mn–mg high pressure die casting alloy, Mater. Sci. Eng. A 783 (2020) 139280, https://doi.org/10.1016/j.msea.2020.139280.